9

MEMS/NEMS Devices

Two challenges are discussed that involve room-temperature, micro- and nanoscopic semiconductor structures and utilize the thermally-sustained electric fields of p-n junctions. Analytic calculations and numerical simulations support the feasibility of these devices.

9.1 Introduction

This chapter is concerned with two experimentally-testable solid-state second law challenges that can operate at room temperature and which could, in principle, have commercial applications [1, 2, 3]. These are based on the cyclic electrome-chanical discharging and thermal recharging of the electrostatic potential energy inherent in the depletion region of a standard solid-state p-n junction. Essentially, the depletion region can be considered a thermally-rechargable capacitor which, in these incarnations, are used to power either a linear electrostatic motor (LEM) or a high-frequency, MEMS/NEMS[1], double-cantilever resonant oscillator. Numerical results from a commercial semiconductor device simulator (Silvaco International – Atlas) verify primary results from one dimensional analytic models. Present day micro- and nanofabrication techniques appear adequate for laboratory tests of principle. Experiments are currently being planned. The initial impetus to

---

[1]Micro-Electro-Mechanical Systems/ Nano-Electro-Mechanical Systems

explore such devices was given in 1995 by J. Bowles, who noted that solid state and plasma physics are kissing cousins; hence, there should be solid-state analogs to the previously proposed plasma paradoxes (Chapter 8) [4, 5, 6].

As detailed in this monograph, a number of concrete, experimentally-testable second law challenges have been proposed, some of which have been corroborated by laboratory experiments. No experiment has yet demonstrated actual violation, however, since in all cases the entropy generated by experimental apparatus (e.g., heaters/coolers, vacuum pumps) has always exceeded the theoretical maximum reduction in entropy that could be achieved by the proposed negentropic process itself. The present solid-state challenges appear different in this respect: whereas other challenges purport the *potential violability* of the second law, they offer no practical hope of *actual violation* under everyday terrestrial conditions. These solid state challenges, on the other hand, make positive claims on both, for, whereas previous challenges are viable only under extreme thermodynamic conditions (e.g., high temperatures ($T \geq 1000$K), low temperatures ($T \leq 100$K), or low pressure ($P \leq 1$ Torr)), the present systems should be viable at room temperature and pressure and they do not require ancillary entropy-generating apparatus.

This chapter is organized as follows. In §9.2 the physics of p-n junctions and thermally-charged capacitors — which undergird the solid-state challenges — is introduced and developed via one-dimensional analytical models and numerical simulations. In §9.3, a linear electrostatic motor (LEM) is discussed. It is substantiated three ways: via a 1-D analytical model, by analogy with an R-C network, and through 2-D numerical simulations. The device is shown to be viable within a broad range of realistic physical parameters. In §9.4, a resonant double-cantilever oscillator (*hammer-anvil*) is developed along similar lines as for the LEM. Finally, in §5, prospects for laboratory experiments are briefly considered.

9.2 Thermal Capacitors

9.2.1 Theory

The present challenges are based on the physics of the standard p-n junction diode [7, 8]. At equilibrium, the depletion region of a diode represents a minimum free energy state in which bulk electrostatic and diffusive forces are balanced. It follows that when individual n- and p- materials are joined, there is a transient current (due to rapid charge carrier diffusion) and energy release as a depletion region forms and equilibrium is attained. Space charge separation gives rise to a built-in potential (typical values, $V_{bi} \sim 0.5-1$V) and an internal electric field which arrests further charge diffusion. Typical depletion regions are narrow, ranging from $10\mu m$ for lightly-doped semiconductor to $0.01\mu m$ for heavily-doped ones. Although these distances are small, the broadest depletion regions have scale lengths visible to the naked eye and the narrowest are two orders of magnitude larger than atoms. They are large enough to interact with some present-day and many envisioned micro- and nano-scale devices [9, 10]. The thermally-generated electrostatic potential energy of the depletion region fuels this challenge. Practically speaking, a semiconductor
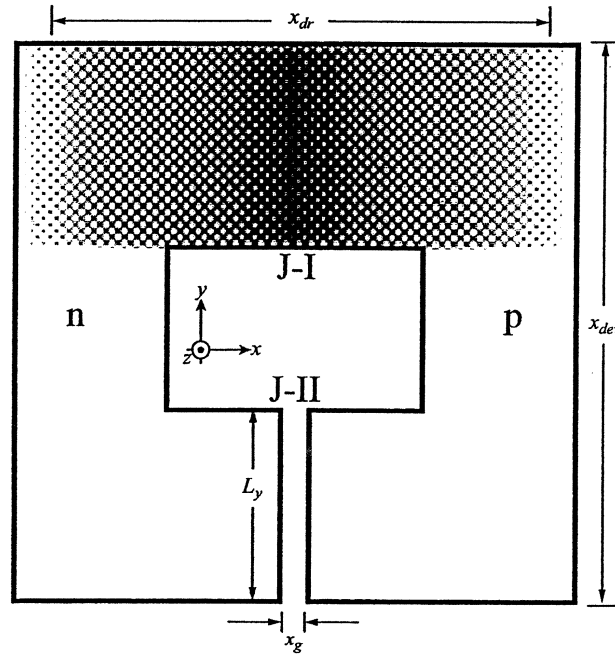
Figure 9.1: *Standard device* with Junctions I and II and physical dimensions and standard coordinates indicated. Depletion region at Junction I is shaded.

depletion region constitutes a thermally-charged capacitor. Whereas standard capacitors dissipate their electrostatic energy through internal parasitic resistance (R_i) on a timescale $\tau \sim R_i C$, thermal capacitors can remain energized indefinitely; they can also recharge thermally under appropriate circumstances.

Consider a p-n device (Figure 9.1) consisting of two symmetric horseshoe-shaped pieces of n- and p-semiconductor facing one another. At Junction I (J-I), the n- and p-regions are physically connected, while at Junction II (J-II) there is a vacuum gap whose width (x_g) is small compared to the scale lengths of either the depletion region (x_{dr}) or the overall device (x_{dev}); that is, $x_g \ll x_{dr} \sim x_{dev}$. Let the n- and p-regions be uniformly doped and let the doping be below that at which heavy-doping effects such as band gap narrowing are appreciable. The p-n junction is taken to be a step junction; diffusion of donor (D) and acceptor (A) impurities is negligible; the depletion approximation holds; impurities are completely ionized; the semiconductor dielectric is linear; and the system operates at room temperature. For a silicon device as in Figure 9.1, representative physical parameters meeting the above conditions are: $N_A = N_D = 10^{21}$ m^{-3}, $x_{dev} = 10^{-6}$ m on a side, $x_{dr} = 1.2 \times 10^{-6}$ m, and $x_g = 3 \times 10^{-8}$m. This dopant concentration results in a built-in potential of $V_{bi} \simeq 0.6$ V. For the discussion to follow, the p-n device (Figure 9.1) with these parameters will be called the *standard device*.

Standard one-dimensional formulae have been used to estimate V_{bi} and x_{dr} [7, 8]:

$$V_{bi} = \frac{kT}{q} \ln\left(\frac{N_A N_D}{n_i^2}\right) \tag{9.1}$$

and

$$x_{dr} = \left[\frac{2\kappa\epsilon_o V_{bi}}{q} \frac{(N_A + N_D)}{N_A N_D}\right]^{\frac{1}{2}} \tag{9.2}$$

Here kT is the thermal energy; q is an electronic charge; n_i is the intrinsic carrier concentration of silicon ($n_i \simeq 1.2 \times 10^{16}$ m^{-3} at 300K); ϵ_o is the permitivity of free space; and $\kappa = 11.8$ is the dielectric constant for silicon.

That an electric field exists in the J-II gap at equilibrium can be established either via Kirchhoff's loop rule (conservation of energy) or via Faraday's law. Consider a vectorial loop threading the J-I depletion region, the bulk of the standard device, and the J-II gap. Since the electric field in the J-I depletion region is uni-directional, there must be a second electric field somewhere else along the loop to satisfy Faraday's law ($\oint \mathbf{E} \cdot d\mathbf{l} = 0$). An electric field elsewhere in the semiconductor bulk (other than in the depletion region), however, would generate a current, which contradicts the assumption of equilibrium. Therefore, by exclusion, the other electric field must exist in the J-II gap. Kirchhoff's loop rule establishes the same result. Conservation of energy demands that a test charge conveyed around this closed path must undergo zero net potential drop; therefore, to balance V_{bi} in the depletion region, there must be a counter-potential somewhere else in the loop. Since, at equilibrium, away from the depletion region there cannot be a potential drop (electric field) in the bulk semiconductor – otherwise there would be a nonequilibrium current flow, contradicting the assumption of equilibrium – the potential drop must occur outside the semiconductor; thus, it must be expressed across the vacuum gap.

In Figure 9.2, the energy ($\mathcal{E}$), space charge density (ρ), and electric field ($\mathbf{E}$) are depicted versus horizontal position (x) through J-I and J-II. There are several important differences between the two junctions. The most noticable is that, while physical properties vary continuously with position across the J-I region, there are marked discontinuities for J-II. These are due to the inability of electrons to jump the vacuum gap (x_g). This restricts the diffusion of charge carriers that would otherwise spatially smooth the physical properties. As a result, Junction II suffers discontinuities in energies, voltages and space charge. Because the J-II gap is narrow and the built-in potential is discontinuous, there can be large electric fields there, more than an order of magnitude greater than in the J-I depletion region. Treating the gap one-dimensionally, the J-II electric field is uniform, with $|\mathbf{E_{J-II}}| \simeq \frac{V_{bi}}{x_g}$, while in the J-I bulk material it has a triangular profile, with average magnitude $|\mathbf{E_{J-I}}| \sim \frac{V_{bi}}{x_{dr}}$. The ratio of the electric field strength in the J-II gap to that in the middle of the J-I depletion region scales as $\frac{\mathbf{E_{J-II}}}{\mathbf{E_{J-I}}} \sim \frac{x_{dr}}{x_g} \gg 1$. For the *standard device*, the average value of the field strength is $|\mathbf{E_I}| \sim \frac{0.6V}{1.2 \times 10^{-6}m} \simeq 5 \times 10^5$ V/m and $|\mathbf{E_{II}}| \sim \frac{0.6V}{3 \times 10^{-8}m} \sim 2 \times 10^7$ V/m, rendering $\frac{\mathbf{E_{J-II}}}{\mathbf{E_{J-I}}} \sim 40$.

Let a switch bridge the J-II gap, physically connecting the entire facing surfaces of the n- and p-regions. For the present discussion, let the switching element be
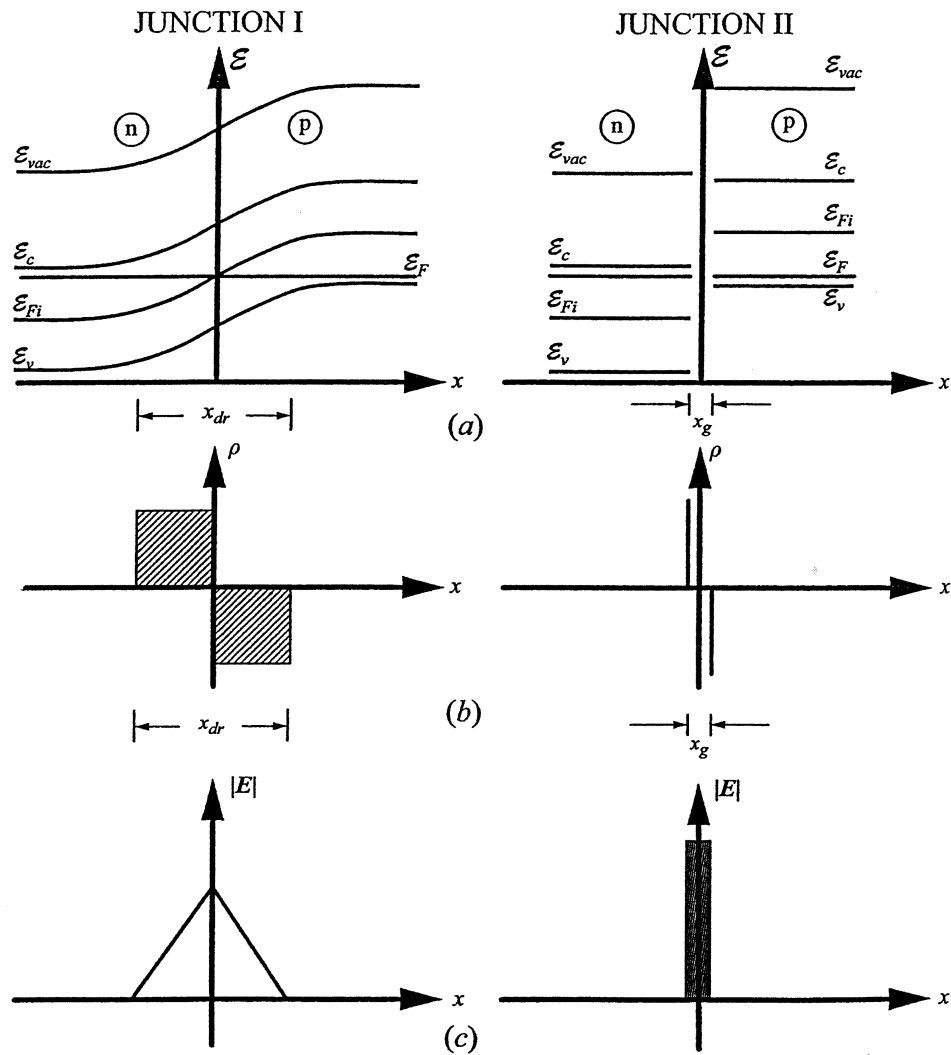
Figure 9.2: Physical characteristics versus position x through Junctions I and II. Left $(x < 0)$ and right $(x > 0)$ sides of each graph corresponds to n- and p-regions, respectively. (a) Energy levels for vacuum $(\mathcal{E}_{vac})$, conduction band edge $(\mathcal{E}_c)$, intrinsic Fermi level $(\mathcal{E}_{Fi})$, Fermi level $(\mathcal{E}_F)$, valence band edge $(\mathcal{E}_v)$. (b) Charge density (ρ). (c) Electric field magnitude $(|\mathbf{E}|)$ Note that vertical scales for $\mathbf{E}$ are different for J-I and J-II $(|\mathbf{E_{J-II}}| \gg |\mathbf{E_{J-I}}|)$.

simply a slab of intrinsic semiconductor inserted into the J-II gap. If the current transmission through the slab is good (that is, its effective resistance and junction potentials are small), then when equilibrium is reached, the physical characteristics of J-II will be approximately those of J-I, as depicted in Figure 9.2.

Theoretical limits to the energy released from J-II during its transition from an open- to a closed-switch configuration can be estimated from the total electrostatic energy $\mathcal{E}_{es}$ inherent to the J-II junction. Let $\Delta\mathcal{E}_{es}(J-II) = [\mathcal{E}_{es}(J-II, open) - \mathcal{E}_{es}(J-II, closed)]$ be the difference in electrostatic energy in J-II between its closed- and opened-switch equilibrium configurations (Figure 9.2). Within the 1-D model constraints, this can be shown to be roughly:

$$\Delta\mathcal{E}_{es}(J-II) \simeq \frac{\epsilon_o}{2}[\frac{x_{dr}kT}{q}\ln(\frac{N_A N_D}{n_i^2})]^2 \cdot [\frac{1}{x_g} - \frac{1}{3}\frac{\kappa}{x_{dr}}], \qquad (9.3)$$

By eliminating V_{bi} and x_{dr} with (9.1) and (9.2) and using $N_A = N_D \equiv N$, (9.3) can be recast into:

$$\Delta\mathcal{E}_{es}(J-II) \simeq \frac{16\kappa\epsilon_o^2}{qN}\{\frac{kT}{q}\ln[\frac{N}{n_i}]\}^3\{\frac{1}{x_g} - \frac{2}{3}\kappa(\frac{2\kappa\epsilon_o}{Nq}(\frac{kT}{q})\ln[\frac{N}{n_i}])^{-1/2}\} \qquad (9.4)$$

It is evident from (9.4) that the device's energy varies strongly with temperature, scaling as $(T)^3$. This is not surprising since primary determinants of the energy are V_{bi} and x_{dr}, both of which originate from thermal processes.

Positive energy release ($\Delta\mathcal{E}_{es} > 0$) is subject to limits in x_g, N, and T. From (9.3), an energy crossover ($+\Delta\mathcal{E}_{es}$) to ($-\Delta\mathcal{E}_{es}$) occurs at $x_g = \frac{3}{\kappa}x_{dr}$; for silicon, this is $x_g \simeq \frac{x_{dr}}{4}$. That is, only for $x_g \leq \frac{x_{dr}}{4}$ will net energy be released in switching from open- to closed-gap configurations. Since x_{dr} is normally restricted to $x_{dr} \leq 10^{-5}$m, this implies $x_g \leq 2 \times 10^{-6}$m, thus, thermal capacitors must intrinsically be microscopic in the gap dimension; and, at least for the vacuum case, mechanical considerations will probably also similarly limit the other two dimensions. Equation (9.4) indicates that energy crossover for N occurs for the *standard device* at $N \sim 10^{22}$m^{-3}. Finally, $\Delta\mathcal{E} \longrightarrow 0$ when T falls below the freeze-out temperature for charge carriers; for silicon, $T_{freeze} \leq 100$K.

For the *standard device*, (9.3) predicts the J-II region contains roughly three times the electrostatic potential energy of the J-I region. Equivalently, the whole p-n device contains twice the energy in its open-gap configuration as it does in its closed-gap configuration and the majority of this excess energy resides in the electric field of the open J-II vacuum gap.

The energy release in closing the J-II gap is equivalent to the discharge of a capacitor. For the *standard device*, (9.3) gives the net energy release as $\Delta\mathcal{E}_{es}(J-II) \sim 5.2 \times 10^{-17}$J ~ 320 eV. When J-II is open, there are about 330 free electronic charges on each gap face (calculable from Gauss' law); when it is switched closed, most of these disperse through and recombine in the J-II bulk. This net flow of charges is due to particle diffusion powered by concentration gradients and to particle drift powered by the large capacitive electric field energy of the open J-II vacuum gap. Thermodynamically, this energy release may be viewed as simply the relaxation of the system from a higher to a lower energy equilibrium state.

This thermal capacitor can remain charged indefinitely (until discharge) since the open-gap configuration is an equilibrium state of the system.

The device output power P_{dev} scales as: $P_{dev} \sim \frac{\Delta\mathcal{E}_{es}(J-II)}{\tau_{dis}}$, where τ_{dis} is the characteristic discharging time for the charged open-gap J-II region as it is closed. If τ_{dis} is short, say $\tau_{dis} \simeq 10^{-7} - 10^{-8}$ sec – a value consistent with the size of micron-sized p-n junctions or typical inverse slew rates of micron-sized transistors – then the instantaneous power for a single, switched *standard device* should be roughly $P_{dev} \simeq 0.5 - 5 \times 10^{-9}$ W. Instantaneous power densities can be large; for the *standard device* it is on the order of $\mathcal{P}_{dev} = \frac{P_{dev}}{(10^{-6}m)^3} \sim 0.5 - 5 \times 10^9$ Wm^{-3}.

9.2.2 Numerical Simulations

Two-dimensional numerical simulations of this system were performed using Silvaco International's semiconductor Device Simulation Software [Atlas (S-Pisces, Giga)]. Junctions were modeled as abrupt and the physical parameters for charge carriers were generic. Output from the simulations were the two-dimensional, steady-state, simultaneous solutions to the Poisson, continuity, and force equations, using the Shockley-Read-Hall recombination model. There is good agreement between the results of the 2-D simulator and those of the 1-D analytic model.

Devices identical to and similar to the *standard device* were studied. Over a wide range of experimental parameters ($10^{17} \leq N_{A,D} \leq 10^{26}$m^{-3}; $10^{-8} \leq x_g \leq 3 \times 10^{-7}$m), the two-dimensional numerical simulations showed good agreement with the primary findings of the 1-D analytic model, most significantly that much larger electric fields reside in the J-II vacuum gap than in the J-I junction, and that significant electrostatic energy is both stored in the J-II region and is released upon switching. Their differences can be traced primarily to the unrealistic discontinuities in physical parameters in the 1-D model, which were smoothed by the more realistic 2-D simulator.

In Color Plate IV, the electric field magnitude is shown for three related variations of the *standard device*. Color Plate IVa (hereafter, Case 1) depicts the electric field for the *standard device*, with the J-II gap closed. As expected, the electric fields are modest ($|\mathbf{E}| \leq 10^6$ V/m) and are centered on the depletion regions, which, as predicted in the 1-D model, extend over the length of the device. The field structure demonstrates perfect symmetry with respect to its horizontal mirror plane and rough mirror symmetry with respect to its vertical mirror plane. The imperfect vertical mirror symmetry is due to the differences in the physical properties of the charge carriers.

Color Plate IVb (Case 2) depicts the electric field magnitude for the *standard device*. While the electric fields in the J-I depletion regions of Cases 1 and 2 are similar, in the J-II regions they are significantly different. The J-II electric field in Case 2 is $E \sim 7 \times 10^6$ V/m versus an average of $E \sim 5 \times 10^5$ V/m for Case 1. Numerical integration of the electrostatic field energy over the entire region (vacuum and bulk) indicates the total electrostatic energy of Case 2 is roughly 1.5 times that of Case 1. Considering only the J-II region of each device, Case 2 stores roughly twice the electrostatic energy of Case 1. These are within 50% of the the energy estimates of the 1-D analytic model.
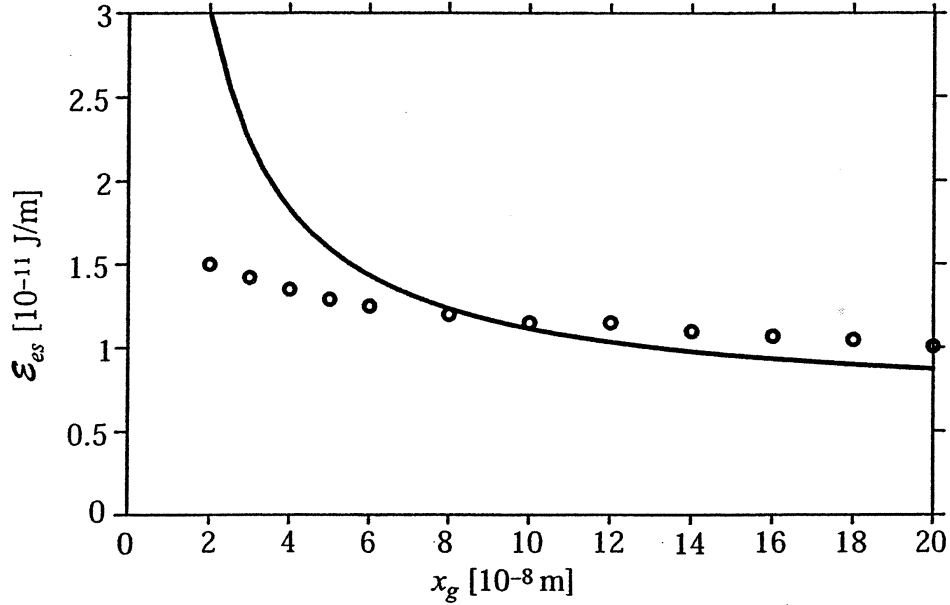
Figure 9.3: Z-normalized electrostatic potential energy $\mathcal{E}_{es}$ versus gap width (x_g) for *standard device* in 1-D model (solid line) and 2-D model (open circles).

Color Plate IVc depicts Case 3, a configuration intermediate between Cases 1 and 2, and one in which the J-II gap of the *standard device* is 20% bridged at its center by a slab of undoped silicon ($l_x = 300\mathring{A}$, $l_y = 600\mathring{A}$). As expected, the bridge allows electron-hole transport between the n and p regions, thereby reducing the large fields of Case 1 closer to values of Case 2. The field is attenuated most across the bridge, but in fact, attenuation extends over the entire length of the channel (L_y). The electrostatic energy of Case 3 is intermediate between Cases 1 and 2. This can be viewed as partial shorting out of the thermal capacitor. The electric fields for all cases are primarily in the x-direction, and especially so for Case 2.

Electrostatic potential energy is stored in the J-I and J-II regions of the device in both the open- and closed-gap configurations. In Figure 9.3, $\mathcal{E}_{es}$ is plotted versus x_g for the *standard device*, comparing the 1-D and 2-D models. (Note that the energy is normalized here with respect to the z-direction (J/m) so as to conform with the output of the 2-D model.) The total electrostatic energy is the sum of the contributions from the vacuum energy density $(\frac{\epsilon_o E^2}{2})$ and n-p bulk energy density $(\frac{\kappa \epsilon_o E^2}{2})$, integrated over their respective regions. In the 1-D model, we take the electric field in the J-II gap to be constant, while in the J-I region it is taken to have a triangular profile as in Figure 9.2, with maximum electric field strength of $E_{max} = \frac{2V_{bi}}{x_{dr}}$. For both models, the device energy decreases
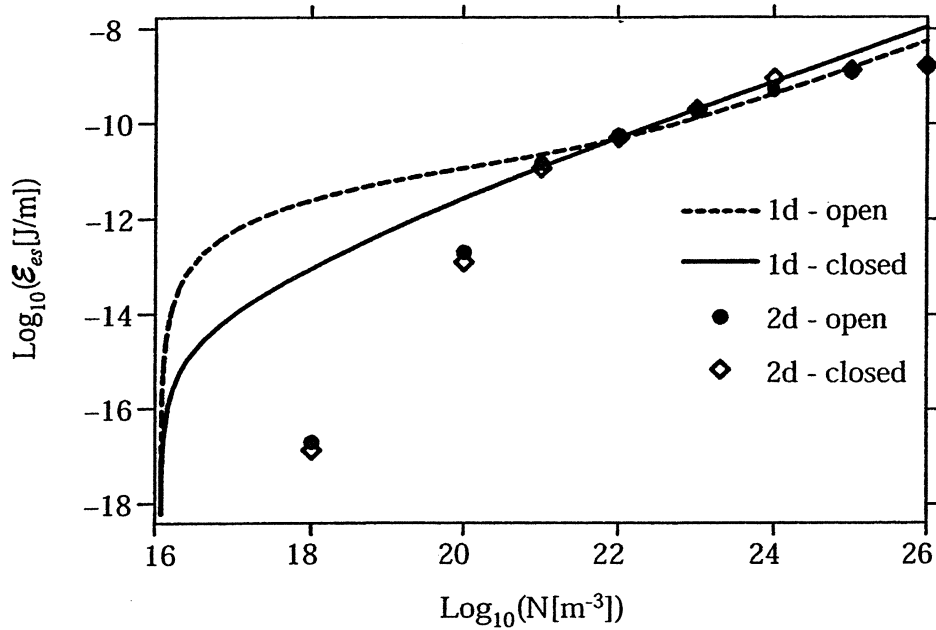
Figure 9.4: Z-normalized electrostatic energy $\mathcal{E}_{es}$ versus dopant concentration (N) for *standard device* for open- and closed-gap configurations. Comparison of 1-D and 2-D models.

monotonically with increasing gap width, however their magnitudes and slopes differ due to the differing model assumptions. At small gap widths ($x_g \leq 10^{-7}$m), the 1-D model predicts greater energy than the 2-D model, owing principally to its vacuum energy, however, at larger gap widths ($x_g \geq 10^{-7}$m) the energy in the 2-D model's n-p bulk dominates, as will be shown later. The 1-D model explicitly ignores contributions of energy to the open-gap configuration arising from the p-n bulk semiconductor on either side of the gap. (See (9.3).) In the density vicinity of the *standard device* the two models agree to within about 50%.

The stored electrostatic potential energy of the device strongly depends upon the dopant concentration. In Figure 9.4, $\mathcal{E}_{es}$ is plotted for the *standard device* versus dopant concentration N, for both open- and closed-gap configurations, comparing 1-D and 2-D models. Above $N = 10^{18}$m^{-3} the 1-D model shows roughly constant logarithmic increase in $\mathcal{E}_{es}$ with increasing N, while the 2-D model shows a roughly constant logarithmic increase up to about $N \simeq 10^{21}$m^{-3}, at which point $\mathcal{E}_{es}$ begins to flatten out and saturate for both open- and closed-gap configurations.

Both models display a crossover in energy between the open-gap and closed-gap configuration (See Color Plate IV) above the dopant concentration of the *standard device* ($N = 10^{21}$m^{-3}). The crossover density N_{cross} is where $\Delta\mathcal{E}_{es}$ reverses sign. In the 2-D model the energy crossover occurs at $N_{cross} \simeq 7 \times 10^{22}$m^{-3}, while in the 1-D model it occurs at $N_{cross} = 8 \times 10^{21}$m^{-3}. Above N_{cross} the closed-gap
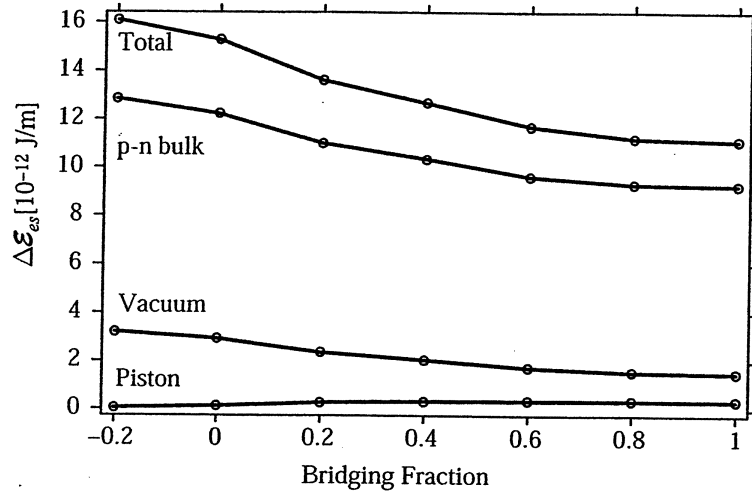
Figure 9.5: Z-normalized electrostatic energies $\mathcal{E}_{es}$ versus gap bridging fraction by undoped silicon slab.

configuration is more energetic than the open-gap one. As a result, above N_{cross} one cannot expect to extract energy by closing the J-II gap. The *standard device* operates at $N = 10^{21} \mathrm{m}^{-3}$, which is a factor of 8 below the 1-D crossover and a factor of 70 below the 2-D crossover density.

Energy release due to gap closing can be made continuous. Let a tightly fitting rectangular slab of silicon be inserted into the gap, thereby allowing the transport of charge between the separated n- and p-regions and the relaxation of the J-II region into an equilibrium state like J-I (Figure 9.2). Figure 9.5 displays the electrostatic energy of the *standard device* ($\mathcal{E}_{es}$) versus bridging fraction by a slab of undoped silicon ($x_g = 300\mathring{A} \times 3000\mathring{A} = L_y$). Here, 0% bridging corresponds to a completely open configuration and 100% bridging corresponds to a completely closed configuration.

As expected, the total system, vacuum, and bulk energies decrease as the silicon is inserted; the silicon bridge energy increases slightly with its insertion. At full insertion, the system's energy is partitioned between bulk, vacuum and piston energy in a ratio of roughly 6 : 1 : 0.25. These data suggest that for minimal investment in piston energy, roughly 10 times more energy is released in the device as a whole. The 2-D simulations indicate a faster-than-linear decrease in system energy with bridging fraction. This can be explained by diffusion of charge into the bulk, ahead of the silicon slab.

9.3 Linear Electrostatic Motor (LEM)

9.3.1 Theory

The 1-D analytic and the 2-D numerical models verify that significant electrostatic potential energy resides in the J-II region of the *standard device* and that it can be released when the device is switched from an open to a closed configuration. Both configurations (Cases 1 and 2 in Color Plate IV) represent equilibrium states; that is, these are states to which the device relaxes when left alone in a heat bath. Their energies are different because of their differing boundary conditions, specifically in the J-II gap, which frustrates the diffusive transport of electrons and holes between the n- and p-regions. Since each configuration is a state to which the system naturally thermally relaxes, the device may be made to cycle between Cases 1 and 2 simply by opening and closing (bridging) the J-II gap with a piston (as done in Figure 9.5). Many energy extraction schemes can be imagined; here we consider one that can be rigorously analysed: a linear electrostatic motor (LEM).

The motor consists of a dielectric piston in the J-II gap which is propelled by a self-generated, electrostatic potential energy minimum (pulse). This electrostatic pulse propagates back and forth through the channel, carrying the piston with it. The piston itself creates the potential energy minimum in which it rides by electrically bridging the J-II gap locally. The free energy that drives the piston resides in the gap electric field; its thermal origin was discussed earlier (See (9.4).). In essence, the piston perpetually 'surfs' an electrostatic wave that it itself creates. As will be shown, the piston can surf under load (thus performing work) in the presence of realistic levels of friction and ohmic dissipation. In accord with the first law of thermodynamics, the net work performed must come from the surrounding heat bath; however, if the first law is satisfied, then the second law is compromised.

Consider a dielectric slab piston situated outside a charged parallel plate capacitor, as in Figure 9.6a. Let its motion be frictionless. It is well known that the dielectric slab will experience a force drawing it between the capacitor plates; this is indicated by the accompanying force diagram, which gives the force density experienced by the dielectric at a given horizontal position. The force can be calculated either by integration of the $(\mathbf{p} \cdot \nabla)\mathbf{E}$ force over the piston volume, or equivalently, by invoking the principle of virtual work since the total energy of the the piston-capacitor system is reduced as the slab enters the stronger field region between the plates. As the force diagram indicates (Figure 9.6a), the piston experiences a force only so long as it in the inhomogeneous field near the end of the capacitor. Specifically, the y-force (F_y) requires gradients in the y-component of the electric field; i.e., $[(\mathbf{p} \cdot \nabla)\mathbf{E}]_y = F_y = (p_x \frac{\partial}{\partial x} + p_y \frac{\partial}{\partial y})E_y$.

Now let the stationary dielectric piston be situated symmetrically between two identical capacitors (Figure 9.6b). Here the net force on the piston is zero and it rests at equilibrium. However, as the accompanying force diagram indicates, this equilibrium is unstable since any infinitesimal y-displacement increases the net force on the piston in the direction of its displacement, while simultaneously reducing the net force in the opposite direction. As a result, the piston will accelerate in the direction of its initial displacement.

Next, consider Figure 9.6c, which depicts a semiconducting dielectric piston at
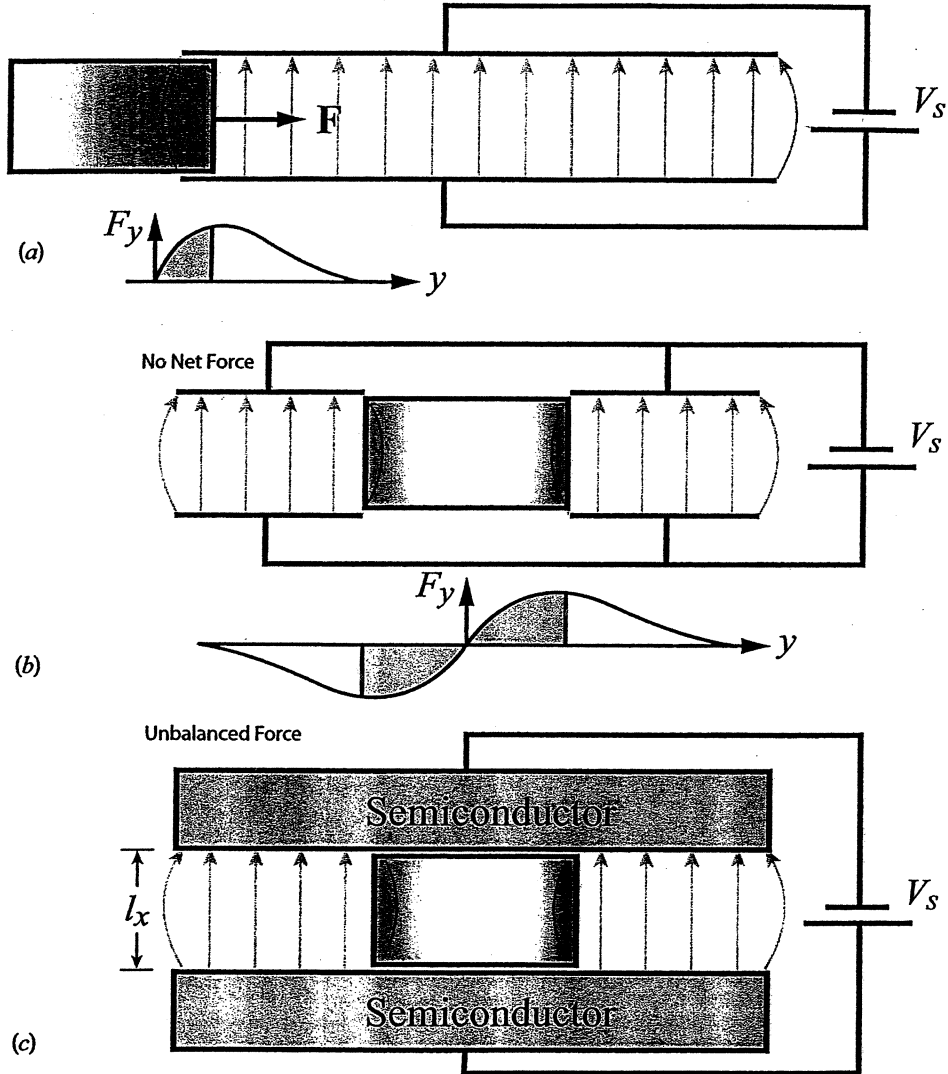
Figure 9.6: Dielectric interacting with capacitors, with accompanying force versus displacement graphs. a) Dielectric piston is drawn into charged capacitor via $[(\mathbf{p} \cdot \nabla)\mathbf{E}]_y$ force. b) Dielectric piston situated equidistantly between two equivalent capacitors in an unstable equilibrium; unbalanced force in direction of displacement. c) Linear electrostatic motor (rail gun): semiconducting dielectric piston in unstable equilibrium between semiconducting capacitor plates.

rest, situated between two semiconductor capacitor plates. (Compare this to Case 3 in Color Plate IV.) The semiconducting dielectric piston allows charge transport between the plates, and so it locally reduces the electric field in and around the piston; thus, the piston sees more intense fields to either side. Essentially, it is in the same unstable equilibrium depicted in Figure 9.6b. If displaced, it will accelerate in the direction of its displacement.

From the principle of virtual work, one can write the frictionless electrostatic acceleration (a_{es}) of the piston (mass density ρ; physical dimensions l_x, l_y, l_z; dielectric constant ϵ) inside a long parallel plate capacitor as

$$a_{es} \simeq \frac{\epsilon - \epsilon_o}{2l_y\rho}(E_1^2 - E_2^2) = \frac{\epsilon - \epsilon_o}{2\rho l_y l_x^2}V_s^2(\alpha_1^2 - \alpha_2^2), \tag{9.5}$$

where E_1 and E_2 are the electric field strengths at the ends of the piston and $\alpha_{1,2} = \frac{E_{1,2}}{E_o}$, where $E_o = \frac{V_s}{l_x}$ is the strength of the undisturbed electric field far from the piston.

If the piston is at rest, then by symmetry $E_1 = E_2$, and there is no acceleration, but if the piston is displaced, then $E_1 \neq E_2$ and the piston accelerates in the direction of motion. In the frictionless case, the piston is unstable to any displacement. In essence, this motor is an electrostatic rail gun, the electrostatic analog of the well-known magnetic rail gun.

We note that $a_{es} \neq 0$ *only* for the case of both a semiconductor capacitor and a semiconductor piston; if either the piston or the capacitor plates are perfectly conducting or perfectly insulating, then $a_{es} = 0$. If the capacitor plates are perfect conductors (approximated by metallic plates), then the plate surfaces must be equipotentials, in which case there cannot be a net electric field difference between the front and back ends of the piston ($E_1 - E_2 = 0$), therefore $a_{es} = 0$. On the other hand, if the plates are perfect insulators, then their surface charges are immobile and the electric field remains the same throughout the capacitor despite any displacement of the piston and again $E_1 - E_2 = 0$. Conversely, if the piston is a perfect conductor, its surfaces must be equipotentials so the electric field at the front and back must be the same ($E_1 - E_2 = 0$), or alternatively, one can say that, as a conductor, electric fields cannot penetrate into the piston interior so as to apply the $[(\mathbf{p} \cdot \nabla)\mathbf{E}]_y$ force, and again there can be no net force exerted on it. Finally, if the piston is an insulator, then charge residing on the capacitor plates cannot flow through it so as to diminish the electric field; again, $E_1 - E_2 = 0$. Thus, it is only when both the piston and the plates have finite, non-zero conductivities that they can act as an electrostatic motor.

Assuming the piston to be a semiconducting ($0 < \sigma < \infty$) dielectric (ϵ), then using Ohm's law ($\mathbf{J} = \sigma\mathbf{E}$), the continuity equation ($\nabla \cdot \mathbf{J} = -\frac{\partial \rho}{\partial t}$), and Gauss' law ($\nabla \cdot \mathbf{E} = \frac{\rho}{\epsilon_o}$), one can describe the acceleration of the piston a_{es} in terms of its electromechanical properties as it locally shorts out the electric field in the channel through which it passes:

$$a_{es} = \frac{\epsilon - \epsilon_o}{2\rho l_y}[\frac{V_s}{l_x}]^2 \exp[-\beta\eta]\{1 - \exp[-\eta]\} = \frac{\epsilon - \epsilon_o}{2\rho l_y}E_o^2 \exp[-\beta\eta]\{1 - \exp[-\eta]\}$$
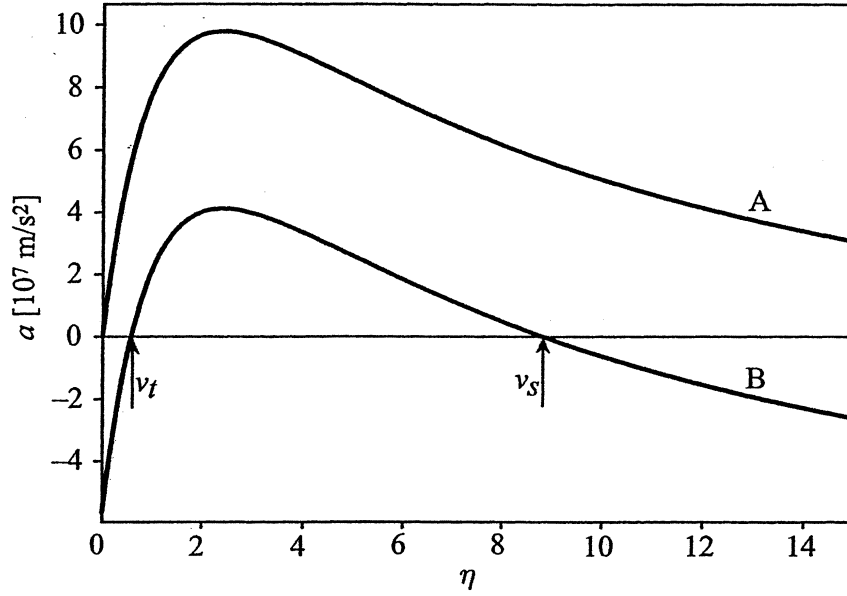
$$\tag{9.6}$$

Figure 9.7: Acceleration of piston a_{es} versus η for *standard device*. Curve A: No friction or load. Curve B: Non-zero friction or load ($a = 5.6 \times 10^7 \text{m/sec}^2$); minimum starting velocity and terminal velocity indicated.

Here $\eta = \frac{2\sigma l_y}{\epsilon v_y}$, v_y is the velocity of the piston, and β is a phenomenological constant that is a measure of how far ahead of the moving piston the electric field is affected. β must be positive to avoid unphysical delta function charge densities. Small β values are evidenced in later 2-D simulations (Plate V); here we take $\beta = 0.1$.

Consider a rectangular slab of silicon ($l_x = 300\text{Å}; l_y = 600\text{Å};\ l_z = 10^4\text{Å}$, $\sigma = 4 \times 10^{-3}(\Omega m)^{-1}$, $\kappa = 11.8$), hereafter called the *standard piston*). In Figure 9.7, the *standard piston*'s acceleration is plotted versus η for the *standard device*. Curve A represents the frictionless case. In the limits of $v_y \to 0$ ($\eta \to \infty$) and $v \to \infty$ ($\eta \to 0$), one has $a_{es} \to 0$, as expected. The former case ($v_y = 0$) has been treated previously. For $v_y \to \infty$, the piston moves too quickly for the capacitor's charge to cross the piston and short out the field, so $E_1 - E_2 = 0$ and $a_{es} = 0$. Since σ and v_y are reciprocals in η, this model also predicts, as before, that $a_{es} = 0$ if the piston is perfectly conducting ($\sigma = \infty$) or perfectly insulating ($\sigma = 0$) and, therefore, accelerates only for the semiconductor case.

The form of a_{es} in (9.6) is handy for introducing friction on, and loading of, the piston. This model considers loading to be constant over the range of velocities of the piston, with the result that its acceleration curves are simply shifted down by an amount equal to the magnitude of the loading. Thus a non-zero start-up velocity and a bounded terminal velocity are imposed on the piston dynamics. We point out that the negative portion of Curve B to the right of v_s does not signify negative acceleration, but simply indicates values of η for which motion is

forbidden.

Numerical integration of (9.6), incorporating friction and load resistances, allows investigation of the piston's complex nonlinear dynamics. For example, in Figure 9.8a, the *standard piston*'s velocity is plotted versus time for three values of friction/loading for the *standard device*. Curve (i) corresponds to the unloaded, frictionless piston case; it has no classically-defined terminal velocity. Curve (ii) corresponds to the piston subject to a constant frictional/load acceleration of 5.6×10^7 m/sec^2. In this case, the piston has a terminal velocity of roughly 8 m/sec. Finally, for Curve (iii) ($a = 9.4 \times 10^7$ m/sec^2 friction/load), the piston has only a narrow range of velocities for which it has positive acceleration; for greater friction or loading the piston does not begin to move.

Figure 9.8c plots piston power versus v_y for the previous three cases. In the frictionless case (Curve (i)), power increases monotonically, but is bounded. Cases (ii) and (iii) display local maxima. The power maximum for case (ii) occurs below its terminal velocity, indicating that the most efficient power extraction schemes should use velocity-governed loads, rather than constant loads. Also, notice that case (ii) and (iii) show initially negative excursions, evidence that energy must be supplied to kick-start the piston's motion.

There are three characteristic times scales pertinent to the operation of the *standard device*: (i) the plate discharge time along the piston ($\tau_{dis} \simeq \frac{l_y}{v_y}$); (ii) the recharging time for the plates (τ_{rec}); and (iii) the period of oscillation of the piston in the channel ($\tau_{osc} \simeq \frac{2L_y}{v_y}$), where v_y is the average velocity of the piston. The discharge time (τ_{dis}) must allow a sufficient difference in electric field to be maintained between the leading and trailing edges of the piston so that it is pulled through the channel.

Circuit theory shows that the recharge time (τ_{rec}) will be longer than the discharge time and should not present an operational problem. Typically, τ_{rec} for p-n diodes of physical dimensions comparable to the *standard device* are $\tau_{rec} \simeq 10^{-7} - 10^{-8}$ sec. However, in order for the electric field in the gap to thermally regenerate enough to maintain force on the piston, the period of oscillation of the piston in the channel (τ_{osc}) must be longer than τ_{rec}, and ideally, much longer. Therefore, for the smooth operation of the motor, the ordering for characteristic time scales should be $\frac{l_y}{v_y} \simeq \tau_{dis} < \tau_{rec} \ll \tau_{osc} \simeq \frac{2L_y}{v_y}$.

The electrostatic motor (Figure 9.9a) can be modeled as a network of discrete resistors and capacitors (Figure 9.9b). The semiconductor capacitor plates are modeled as a distributed network of resistors (R) and their interior surfaces as a sequence of aligned parallel plate capacitors (C). The network is powered by a battery (V_s).

The piston is represented by a resistor and by an accompanying switch. The piston's motion is modeled by the sequential closing and opening of the local switches. As the piston leaves a capacitor$_n$ region, a closed switch$_n$ opens up, while the next switch$_{n+1}$ in line closes, signaling the arrival of the piston. The trailing capacitor recharges while the leading capacitor discharges.

It can be shown from basic circuit theory – and has been confirmed by parametric studies of this system using PSpice network simulations – that the time constant
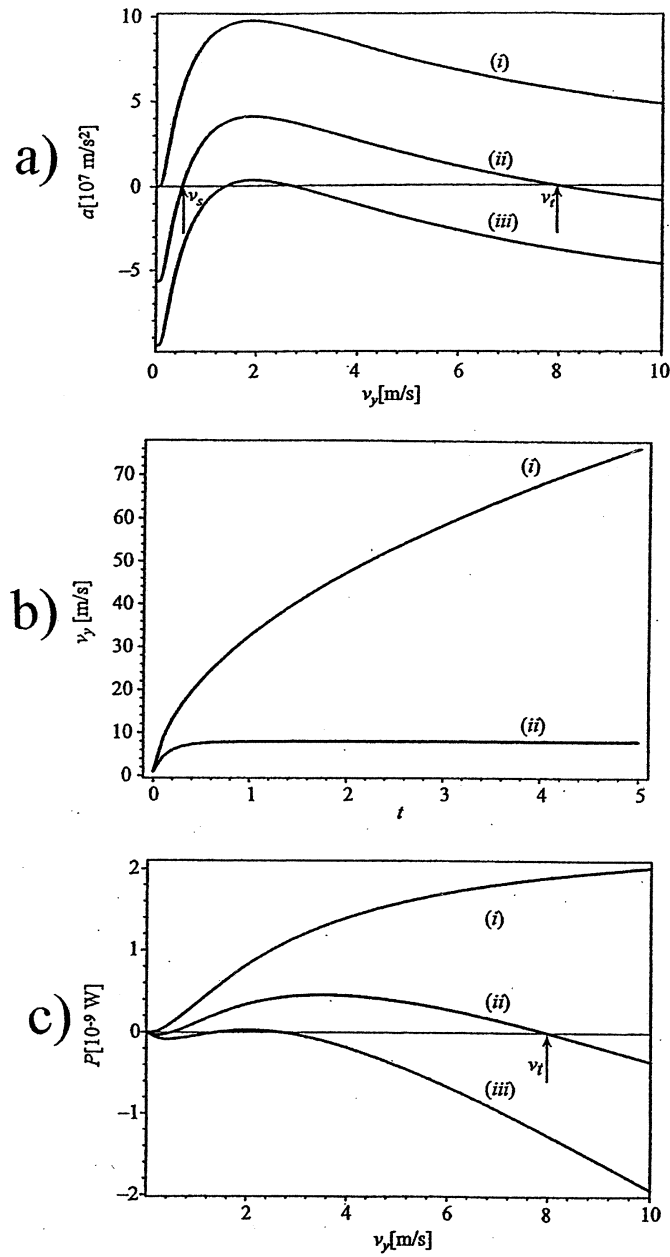
Figure 9.8: Piston dynamics for *standard device*. a) Acceleration versus v_y for three cases: (i) frictionless; (ii) friction/load acceleration $a = 5.6 \times 10^7 \mathrm{m/sec^2}$; and (iii) friction/load acceleration $a = 9.4 \times 10^7 \mathrm{m/sec^2}$. b) Velocity versus time for cases (i) and (ii) above; case (iii) absent for lack of sufficient start-up velocity. c) Piston power versus v_y for cases (i) - (iii) above.
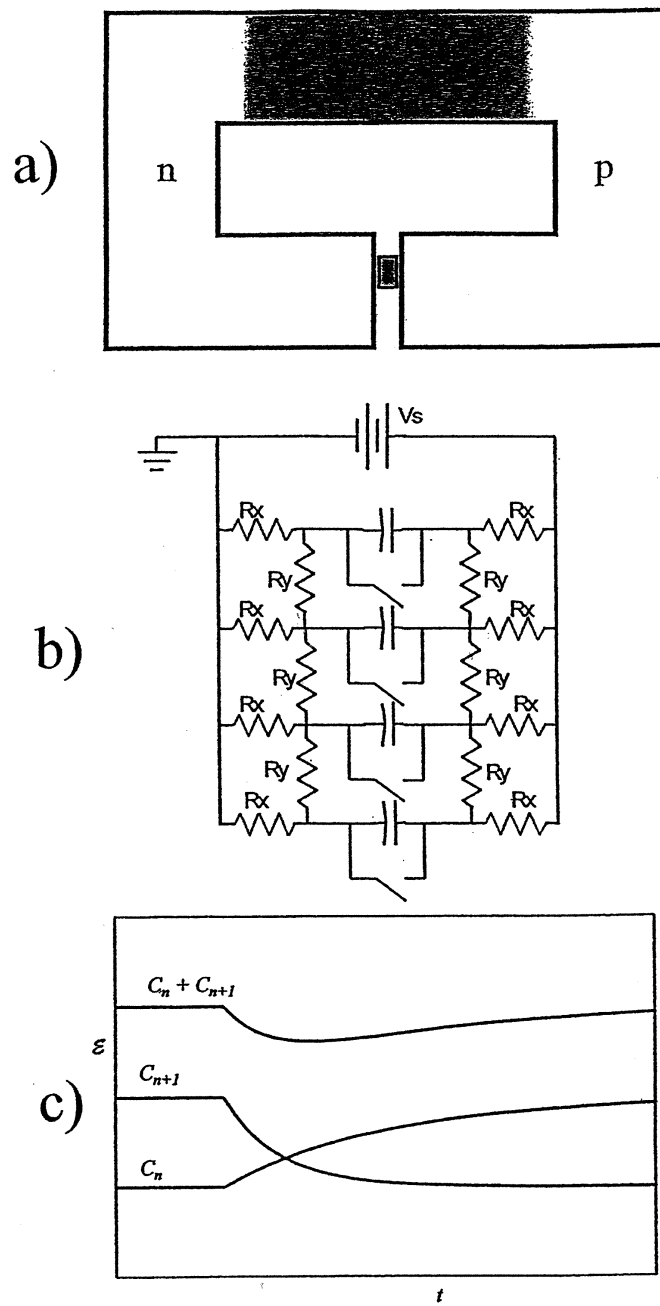
Figure 9.9: Linear electrostatic motor modeled as a discrete resistor-capacitor network. a) Piston in *standard device.* b) Analog resistor-capacitor network model. c) Electrostatic energy versus time for sequential firing of two capacitors; traveling negative potential energy pulse evident in $(C_n + C_{n+1})$ curve.

for the discharging capacitor is less than the time constant for the recharging ca-
pacitor. As a result, the moving piston always finds itself moving in the direction
of more intense electric fields and field gradients. In other words, it perpetually
moves forward toward a lower local energy state, riding in a self-induced potential
energy trough. The traveling piston can also be viewed as the material equivalent
of an electrical pulse propagating through a resistive-capacitive transmission line.
This semiconducting piston acts analogously to the conducting piston in a mag-
netic rail gun which, by completing the circuit between the gun's two electrified
rails, establishes a current and magnetic field by which the resultant Lorentz force
on the piston's current drives the piston along the rails. In the present electrostatic
case, the piston is propelled forward by the greater $(\mathbf{p} \cdot \nabla)\mathbf{E}$ force on its leading
edge.

When the piston reaches the end of the R-C network, where the field ahead
has dropped off, but where field behind has regenerated, the piston reverses its
motion. As a result, it will move cyclically through the network. It is remarkable
that this motion does not require any electronic timing circuitry; instead, the
timing is set by the piston itself. As long as it overcomes friction, the piston will
run perpetually for the life of the battery.

Via the substitution $V_s \rightarrow V_{bi}$, the piston in Figures 9.9 and 9.10 may now be
identified as the semiconductor piston in Case 3 (Plate IVc). The same physics
applies, except that, whereas the free energy for the linear electrostatic motor (rail
gun) above is supplied by a battery, now it is supplied by the free energy of the
thermally-powered p-n depletion region.

9.3.2 Numerical Simulations

Essentials of the above 1-D dynamical nonequilibrium model of the linear electro-
static motor are corroborated by the equilibrium solutions of the 2-D model. Color
Plate V presents a sequence of 2-D equilibrium solutions simulating aspects of the
motion of the piston through the J-II region of the *standard device*. It is strongly
emphasized that this is *not* a dynamical simulation in which the piston is modeled
as moving; rather, these are quasi-static equilibrium configurations of the system
simulated by the Atlas program in which the piston is held at rest at different
locations in the J-II region, despite implicit force imbalances. Nevertheless, much
physics can be inferred by stepping the piston through the channel in this fashion.

In Plate Va, the leading edge of the piston is visible above the J-II channel. The
electric field is fairly uniform in the gap interior ($E \simeq 7 \times 10^6$ V/m), decreasing in
strength at its ends, as expected. As the piston enters the gap, thereby initiating
the bridging of the separated n- and p-regions, the electric field strength falls
throughout the J-II vacuum and p-n bulk regions, but most strongly near the
piston. This substantiates the β term in (9.6). The field and field gradients
are stronger below the piston (in the direction of implied motion) than above it
(outside the channel); as a result, should the piston be free to move, it would be
drawn further into the channel. In Plate Vc, with the piston now squarely within
the channel, the electric fields in and near the piston have been reduced by a factor
of 3 below pre-insertion values, but they remain larger in the channel ahead of the
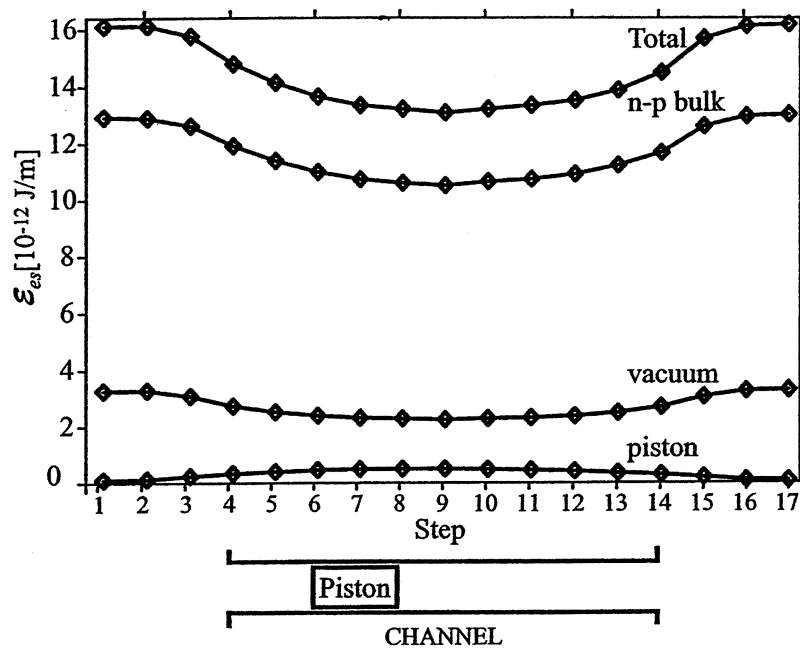
Figure 9.10: Electrostatic potential energy of *standard device* versus piston position in J-II gap: Total energy, p-n bulk energy, vacuum energy, and piston energy indicated. Piston located at Step 7, corresponding to Plate Vd.

piston and, therefore, continue to draw it in.

In Plate Vd, as the piston approaches mid-channel, the field ahead of the piston continues to be more intense than the one behind. At mid-channel, (Plate Ve), the field is roughly balanced on both sides of the piston. Here, a resting piston would experience roughly no net force, but it would be in the unstable equilibrium position depicted in Figure 9.8b. Were it in motion, then it should continue to see stronger fields and field gradients ahead of it than behind it and, thus, would continue to move in the direction of motion. Furthermore, since presumably it has already accelerated to mid-channel from the gap ends, its inertia should carry it past this mid-channel equilibrium point.

Now compare the upper channel in Plates Vd and e. Notice the field has been partially restored between Vd and Ve after the 'passage' of the piston. Finally, in Plate Vf, the piston has reached the bottom of the channel. As before, the field is locally reduced, but it has regenerated behind. Since the field is now stronger behind the piston, it should exert a net force upward so as to reverse its motion. It is instructive to view this 'motion sequence' in reverse, proceeding from Ve→Va so as to appreciate how the piston's motion can be cyclic. This is most evident perhaps in the inversion symmetry seen between Plates Vc and Vf.

Figure 9.10 displays the equilibrium electrostatic potential energies of the *standard device* and *piston* for a sequence of steps through the channel, calculated with

the Atlas 2-D simulator. Frames a, b, c, d, e, and f in Plate V correspond to Steps 1, 3, 5, 7, 9 and 13, respectively, in Figure 9.10. The total, vacuum, and p-n bulk energies of the *standard device* decrease significantly and symmetrically as the piston enters the channel from either direction and reaches the mid-channel (Step 9). The fractional change in field energy in the vacuum is greater than for the p-n bulk, but the greatest absolute change occurs in the bulk. The electrostatic energy invested in the piston itself is small compared with the bulk and vacuum contributions.

The data in Figure 9.10 are equilibrium solutions and assume the piston to be at rest. The energy depression seen in Figure 9.10 would occur only locally around the piston and would be spatially asymmetric, with its greatest strength and gradient in the direction of the piston's motion, both as suggested in individual frames of Plate V, in Figure 9.9c, and in the 1-D analytic model. In summary, the sequential 2-D numerical simulations (Plate V and Figure 9.10) support the 1-D nonequilibrium analyses preceding it.

9.3.3 Practicalities and Scaling

The steady-state operation of this solid-state electrostatic motor constitutes a *perpetuum mobile* of the second type. It pits the first law of thermodynamics against the second. If the piston cycles perpetually while under load, performing work, then this energy must come from somewhere. Assuming the first law is absolute, the only possible source of this unlimited energy must be the [infinite] heat bath surrounding the device. Since the device operates in a thermodynamic cycle, heat is transformed solely into work, in violation of the second law.

This section addresses the practical details of this device, paying especial attention to the operational limits imposed by physically realistic parametric values: mass, physical dimensions, electric field, friction, electrical conductivity, characteristic time scales (e.g., τ_{dis}, τ_{rec}, τ_{osc}), and statistical fluctuations. It is found that there exists a broad parameter space at and below the micron-size scale for which a semiconducting piston should be able to overcome realistic levels of friction and load so as to perform work indefinitely, while being driven solely by the thermally-generated electric fields of a p-n junction. It is found that these devices should be able to convert heat energy into work with high instantaneous power densities, perhaps greater than 10^8 W/m^3.

Consider the *standard piston* situated in the J-II gap of the *standard device*. From Figure 9.10, the *standard piston* should reside in a potential well approximately 3×10^{-18} J deep. From Figures 9.8 and 9.9, in the frictionless case the piston should experience a maximum acceleration of 10^8m/sec^2 and be capable of instantaneous power outputs of 2×10^{-9}W. We will now consider a realistic model for friction.

Let the J-II channel walls be tiled with a thin, low-friction surface such as graphite. Let the outer surfaces of the piston be only partially tiled with a matching low-friction surface such that the contact fraction between the piston and the channel walls (f_c) is small ($0 < f_c \ll 1$). On the other hand, let f_c be sufficiently large that: (i) there are sufficient numbers of atoms projecting out from the piston

surfaces in contact with the channel walls to hold and guide the piston; and (ii) there is sufficiently good electrical conduction between the piston and the channel walls that one can use standard Ohmic current rather than quantum mechanical tunneling current to describe the system's electrical behavior.

It is well known that, at micron and sub-micron size scales, atomic, ionic, and electrostatic forces (e.g., van der Waals' interactions, induced surface charge, molecular and hydrogen bonding, surface tension) can play dominant roles in system dynamics. In order to minimize friction between the piston and channel walls, f_c should be as small as possible. The smallest non-zero coefficients of static and kinetic friction yet measured experimentally are found in nested multi-walled carbon nanotubes (MWNT) [11, 12]. Upper-limit values of coefficients of static (s) and kinetic (k) friction have been experimentally measured to be: $\mathcal{F}_s < 2.3 \times 10^{14}$ N/atom $= 6.6 \times 10^5$ N/m^2, and $\mathcal{F}_k < 1.5 \times 10^{-14}$ N/atom $= 4.3 \times 10^5$ N/m^2. Theoretical arguments suggest true values could be much lower than these. This friction is presumed to arise purely from van der Waals' interactions between the sliding carbon contact surfaces. The friction can be reduced by reducing the contact fraction f_c. Experimental observations suggest that MWNT operate as totally wear-free bearings [13].

The static or kinetic friction $F_{f(s,k)}$ between two surfaces of area A, where normal forces are not imposed and asperities are absent, should scale as: $F_{f(s,k)} = f_c A \mathcal{F}_{(s,k)}$. For the piston in the J-II channel, the acceleration is:

$$a_{f(s,k)} = \frac{F_{f(s,k)}}{m} = \frac{f_c A \mathcal{F}_{(s,k)}}{\rho_{Si} l_x l_y l_z} = \frac{2 f_c \mathcal{F}_{(s,k)}}{\rho_{Si} l_x} \qquad (9.7)$$

For the piston to begin moving in the channel the electrostatic acceleration must exceed the static friction:

$$\frac{a_{es}}{a_{f,s}} = \frac{(\epsilon - \epsilon_o) V_{bi}^2 (\alpha_1^2 - \alpha_2^2)}{4 l_x l_y f_c \mathcal{F}_s} > 1 \qquad (9.8)$$

This inequality is the starting point for delimiting a viability regime for the operation of this device. For the *standard piston* in the *standard device* (letting $\mathcal{F}_s$ be the upper-limit value for MWNT and taking $((\alpha_1^2 - \alpha_2^2) \simeq 0.5)$, (9.8) reduces to:

$$\frac{a_{es}}{a_{f,s}} \simeq (3.2 \times a^{-18}) \frac{1}{l_x^2 f_c} \qquad (9.9)$$

In Figure 9.11 is plotted $\text{Log}_{10}(\frac{a_{es}}{a_{f,s}})$ versus l_x for various contours of constant f_c. For $\text{Log}_{10}(\frac{a_{es}}{a_{f,s}}) < 0$, the frictional acceleration exeeds the electrostatic acceleration, so the piston cannot move. This places a lower bound on the viability regime of the *standard device*. Above this bound, the piston can experience sizable accelerations, on the order of $10^7 - 10^8$ m/sec^2, but these accelerations are still within mechanical strength limits for small structures.

A left-most viability bound for the *standard device* is found by requiring that l_x significantly exceed the size of individual atoms and, preferably, be large enough that the system can be treated by classical, rather than quantum, theory. If the piston thickness l_x is greater than about 50-100 atoms, or about 10^{-8}m, this
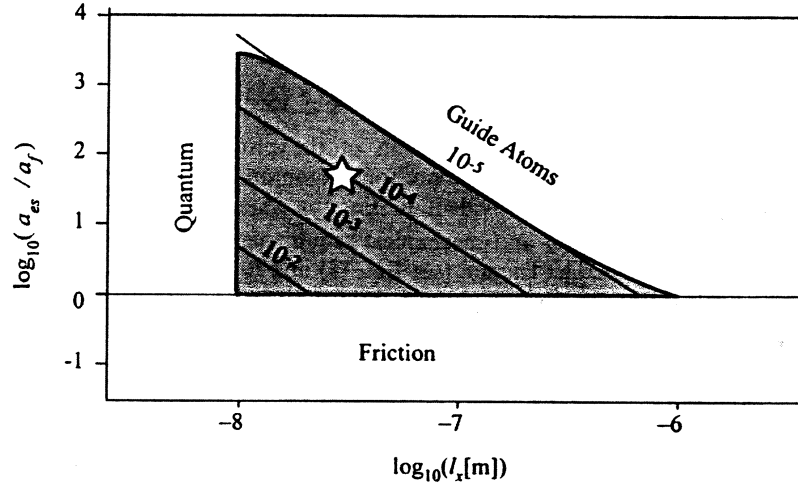
Figure 9.11: Ratio of piston acceleration to frictional acceleration ($\text{Log}_{10}(\frac{a_{es}}{a_f})$)) versus gap width ($x_g$) with contours of constant f_c indicated. Viability regime delimited by labeled boundary lines. Star indicates location of *standard device.*

system should be essentially classical. This criterion sets the left-most bound of the viability regime in Figure 9.11. The last bound is set by restricting f_c such that some reasonable minimum number of atoms act as guide surfaces between the piston and the channel walls. Choosing 10 atoms/piston face as sufficient, the sigmoidal right-top viability bound is determined. This bound can later be modified to satisfy electrical conductivity constraints.

The viability regime has been delimited using realistic, but conservative, choices for the system parameters. More liberal choices (e.g., letting $\mathcal{F}_s \rightarrow \mathcal{F}_k$ or ($\alpha_1^2 - \alpha_2^2$) = 0.8) would expand the regime somewhat. Even as it stands, however, the viability regime for the electrostatic motor spans two orders of magnitude in size ($10^{-8}\text{m} \leq l_x \leq 10^{-6}\text{m}$) and over three orders of magnitude in $\frac{a_{es}}{a_{f,s}}$.

Several observations can be made from Figure 9.11:

a) The spontaneous acceleration of the piston by self-generated fields appears possible only for micron and sub-micron pistons. This is especially evident in (9.6) where $a_{es} \sim \frac{1}{l_x^3}$. Given the severe physical and mechanical requirements for positive acceleration against friction (See (9.8) and (9.9), it is not surprising that this phenomenon has not been discovered accidentally.

b) a_{es} can exceed a_f by more than 3 orders of magnitude, thus allowing significant loading of the piston with which to perform work.

c) More frictional contact surfaces appear feasible (up to 10^3 times more frictional than MWNT), without precluding piston motion or loading.
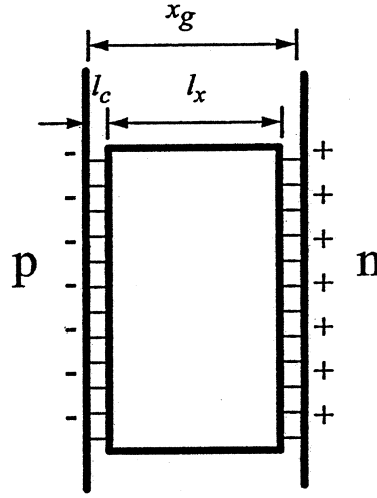
Figure 9.12: Physical dimensions of *standard piston.*

The magnitude of the piston's acceleration ($a_p = a_{es} - a_f$) can be calculated, including friction, using (9.5-9.7). For the *standard device*, using graphitic surfaces and assuming $f_c = 10^{-4}$ (corresponding to 1.7×10^6 atoms on each piston face), one finds $a_f = 1.9 \times 10^6$ m/sec^2, $a_{es} = 6.7 \times 10^7$ m/sec^2, and $a_p = 6.5 \times 10^7$ m/sec^2. The average velocity during a piston stroke is roughly $v_y \simeq \sqrt{2L_y a_p} \simeq 2$m/s. The oscillation period of the piston in the channel is $\tau_{osc} = (\frac{2L_y}{v_y}) \simeq 2 \times 10^{-7}$sec; the oscillation frequency is $f_{osc} = \tau_{osc} \simeq 5 \times 10^6$Hz. τ_{osc} is significantly longer than the typical inverse slew rates for p-n transistors of comparable physical dimensions $(\tau_{dis} \leq \tau_{rec} \sim \tau_{trans} \sim 10^{-8} - 10^{-7}sec<< \tau_{osc} \simeq 2 \times 10^{-7}sec)$; therefore, the electric field in the wake of the piston traversing the channel can recharge before the piston's return. On the other hand, given a typical piston velocity and length $(v_y \simeq 2$m/sec, $l_y \simeq 6 \times 10^{-8}m)$, these field decay rates are sufficiently high for the electric field in the channel walls to decay along the length of the piston $(\tau_{dis} \simeq \frac{l_y}{v_y} \sim 3 \times 10^{-8}sec)$ so as to admit significant difference in the magnitude of the electric field between the leading and trailing edge of the piston; therefore, the *a priori* estimate of $((\alpha_1^2 - \alpha_2^2) = 0.5)$ is plausible. A similar conclusion is supported by evaluation of the exponential decay model (in (9.6)). Overall, the time scale ordering developed earlier $(\tau_{dis} \leq \tau_{rec} \ll \tau_{osc})$ is reasonably well satisfied.

The viability regime depicted in Figure 9.11 is favorable to ohmic treatment of the piston and channel. The piston acts as a sliding electrical resistor – essentially a motor brush – between the positive polarity n-region and the negative polarity p-region, as depicted in Figure 9.12. The piston's electrical resistance can be written as

$$R_{piston} = R_b + 2R_c = \frac{1}{l_y l_z}[\frac{x_g - 2l_c}{\sigma_b} + \frac{2l_c}{f_c \sigma_c}] \simeq \frac{1}{l_y l_z}[\frac{l_x}{\sigma_b} + \frac{2l_c}{f_c \sigma_c}] \qquad (9.10)$$

where $R_{b(c)}[\Omega]$ is the electrical resistance of the piston bulk (contacts); $\sigma_{b(c)}[(\Omega m)^{-1}]$

is the electrical conductivity of the bulk (contact) material; and l_c is the x-length of the contacts. It is assumed that $l_c \ll l_x \simeq x_g$. The values of the l_c and f_c are both small and offset one another, while σ_c can in principle be varied over many orders of magnitude such that R_c can be made negligible compared with R_b. Consider, for example, the *standard device* with a silicon piston lined with graphite, operating with the following parameters: $l_x = 300 \mathring{A}$, $l_y = 600 \mathring{A}$, $l_z = 10^4 \mathring{A}$, $l_c = 5 \mathring{A}$, $\sigma_b = 10\sigma_{Si} = 4 \times 10^{-3} (\Omega m)^{-1}$, $\sigma_c = \sigma_{graphite} = 7.1 \times 10^4 (\Omega m)^{-1}$, and $f_c = 10^{-4}$. With these parameters, one has from (9.6-9.10): $R_b \simeq 10^8 \Omega \gg R_c = 2.5 \times 10^3 \Omega$ and $(a_{es} = 6.7 \times 10^7 \text{m/sec}^2) > (a_p = 6.5 \times 10^7 \text{m/sec}^2) \gg (a_{f,s} = 1.9 \times 10^6 \text{m/sec}^2) > (a_{f,k} = 1.2 \times 10^6 \text{m/sec}^2)$. Ohmic losses for this system, concentrated in the piston region, can be engineered to be insignificant.

For objects in this size range, the effect of statistical fluctuations should be considered, especially since they have been the foil of many past challenges. Earlier analysis indicates the *standard device* can be modeled as an R-C network, so it is appropriate to consider fluctuations in electronic charge. Charge is also naturally salient since it is through charge-induced electric fields that the system is powered. Spectral analysis in the spirit of the Nyquist and Wiener-Khintchine theorems [14] allows one to write the rms charge fluctuation for a resistor capacitor system as $\sqrt{<\Delta Q^2>} = \Delta Q_{rms} \sim \sqrt{4RC^2kT\Delta f}$, where C is capacitance of the J-II region and Δf is the spectral width of the fluctuations measured. Taking characteristic values for the *standard device* ($R = 10^9 \Omega$, $C = \frac{\epsilon_o L_y l_z}{l_x} = 10^{-16}$F, $\Delta f \sim f_{osc} \simeq 5 \times 10^6$Hz, $T = 300$K), one obtains $\Delta Q_{rms} \simeq 2$ electronic charges. Since the total charge in the *standard device's* J-II region is found to be $Q_{total} \simeq 330q$, one expects less than one percent statistical fluctuation in electronic charge over the entire J-II channel capacitor during a piston's oscillation period. Since the fractional statistical fluctuation is much less than the fractional change in charge due to electrical operation of the piston itself ($0.01 \simeq \frac{\Delta Q_{rms}}{\Delta Q_{total}} \ll \frac{\Delta Q_{op}}{\Delta Q_{total}} \simeq 0.4$), by this measure, statistical fluctuations should not play a primary role in the operation of the *standard device*. A similar conclusion can be reached by equating the thermal energy to the piston's kinetic energy.

Assuming that a_{es} is constant in magnitude and that $a_{es} \gg a_f$, the average power per cycle can be shown to be $< P_{sd} >= m_{piston}(2a_p^3 L_y)^{1/2} \simeq 2 \times 10^{-9}$W, where $m_{piston} = \rho_{Si} l_x l_y l_z$ is the mass of the piston. The average power densities for the *standard device* are, therefore, $\mathcal{P}_{sd} \sim 2 \times 10^9$Wm^{-3}. The *standard device* appears capable of producing significant output power and power densities in the presence of realistic levels of friction, while satisfying the conditions for classical electrical conductivity, providing substantial numbers of guide/contact atoms, and overcoming statistical fluctuations.

In Color Plates VIa,b power (W) and power density (Wm^{-3}) are explored for a range of device sizes, scaled in direct physical proportion to the standard device (i.e., $l_y = 2l_x$, $L_y = 5l_y$, $l_z = 33.3l_x$, etc.). The other physical specifications of the *standard device* are retained (i.e., silicon matrix, $N_A = N_D = 10^{21}$m^{-3}, etc.). The previously discussed viability bounds (Figure 9.11) are still enforced. In Plate VIa, the maxima of the power curves (Figure 9.8c) are calculated over an extended viability regime (as in Figure 9.11) and plotted versus l_x and f_c. Power contours extend linearly in value from a maximum of 1.2×10^{-8} W/device (yellow, center)

down to 1×10^{-9} W/device (red). The star indicates the location of the *standard device*.

Perhaps a more meaningful figure of merit than maximum power per device (Plate VIa) is maximum power density (Wm^{-3}). It is a better indicator of how rapidly thermal energy can be transformed into work by a given volume of working substance; thus, it is a better measure of how significantly this device challenges the second law. In Plate VIb, maximum power density (Wm^{-3}) is presented for a range of devices versus f_c and x_g, scaled as before in direct physical proportion to the *standard device*. Whereas in Plate VI the contour values vary linearly with adjacent contours, in Plate VIb they vary logarithmically in value from $10^{10}Wm^{-3}$ (left-most, yellow) to 10 Wm^{-3} (right-most, red). Again, the *standard device* is located by the star. The greatest power density obtains for small devices, while the greatest unit power obtains for larger devices.

The parameter space available for this device (spanned by x_g, x_{dev}, N_A, N_D, T, etc.) is far greater than can be explored here, and only modest attempts have been made to optimize the performance of the *standard device*. Nonetheless, it appears the theoretical instantaneous power densities achievable by it are sizable. To put this in perspective, one cubic meter of *standard devices* (amounting to 10^{18} in number) could, in principle, convert thermal energy into work with instantaneous power output on par with the output of a modern-day nuclear power plant; or, in 1 second, produce the work equivalent of the explosive yield of 500 kg of high-explosive. This, of course, is only *instantaneous* power density since, were the device to convert thermal energy into work at this rate without compensatory heat influx from the surroundings, the device would cool at an unsustainably fast rate of about 100 K/sec.

More advanced designs for the motor can be envisioned. For example, the linear *standard device* could be circularized. This rotary motor would consist of concentric cylinders of n- and p-regions (the stator) joined at their base (to create a depletion region) and having a gap between them in which a multi-piston rotor runs. Multiple rotor pistons could be yoked together so as to balance radial forces and torques. In the limit of large radius, the rotor pistons would move in what is essentially a linear track, so the above discussion for linear motors should apply. The rotor pistons would be driven by the local electric field energy in the cylindrical gap. If they are spaced sufficiently far apart azimuthally, then the field in the wake of a given piston could thermally regenerate in time to power the advancing piston.

9.4 Hammer and Anvil Model

9.4.1 Theory

A more immediate laboratory test of the thermal capacitor concept appears feasible, one sidestepping the high-tolerance micromachining required of the LEM. This will be called the *hammer-anvil*. It is a thermally-charged semiconductor parallel-plate capacitor, with one plate fixed and the other mounted on a flexible double cantilever spring. For mechanical $Q \geq 10^3$, and for matched electrical

and mechanical time constants ($\tau_e \sim \tau_m$), the system can execute steady-state, resonant oscillation by which thermal energy is converted into mechanical energy. An example based on Sandia National Laboratories' SUMMiT^{TM} process is examined, however, more advanced designs are possible. As for the *standard device*, the *hammer-anvil* relies on the depletion region of a n-p junction to establish a potential difference and electric field in the active, open-gap region at the middle of the device. This device can be constructed within present-day NEMS and MEMS fabrication art and so represents a more immediate and cogent challenge than the LEM.

NEMS and MEMS cantilever oscillators have many proven and potential applications, including as accelerometers, motors, clocks, sensors (e.g., temperature, pressure, electronic charge, magnetic fields, environmental contaminants, microbes), beam steerers, choppers, and modulators, computing elements, and switches [15, 16, 17]. These are usually driven by AC electrical signals whose frequencies are commensurate with their mechanical oscillation frequencies, but under suitable circumstances, DC signals can also effectively drive them. Owing to their utility, the art of NEMS-MEMS cantilevers is relatively advanced. DC-driven, resonant micro-cantilevers have been explored [18].

Consider the macroscopic electromechanical device pictured in Figure 9.13a, consisting of a battery (V_o), resistor (R), and a variable capacitor in which the bottom plate (the *anvil*) is fixed, while the top plate (the *hammer*, mass m) is supended from a conducting spring with spring constant k. This will be called the *hammer-anvil*. It is a hybrid of well-known mechanical and LRC oscillators. The hammer is free to move with respect to the anvil and when they contact any accumulated charge on the plates is assumed to flow between them without resistance. The electrical capacitance of the device varies with the dynamic separation of the plates according to

$$C(y) = \frac{\epsilon_o A}{y_{gap} - y}, \tag{9.11}$$

where A is the area of the plates, $y = 0$ is the static mechanical *equilibrium position* of the hammer, y_{gap} is the *equilibrium separation* of the plates, and $y = y(t)$ is the *instantaneous position* of the hammer, with the positive direction downward. For convenience, we denote by $C_o = \frac{\epsilon_o A}{y_{gap}}$ the capacitance when the spring is in its undeflected equilibrium state.

Two independent time constants characterize this system: one electrical ($\tau_e \sim RC_o$) and one mechanical ($\tau_m = 2\pi\sqrt{\frac{m}{k}}$). The electromechanics of the hammer is described by the coupled pair of equations:

$$F = F_{diss} + F_s + F_{es} = m\ddot{y} = -\frac{1}{Q}\dot{y} - ky - \frac{q^2}{2\epsilon_o A}, \tag{9.12}$$

where the instantaneous charge on the plates $q(t)$ satisfies:

$$\dot{q} = (V_o - \frac{q(y_{gap} - y)}{\epsilon_o A})\frac{1}{R}; \quad q < q_{sat}, \tag{9.13}$$

and $\dot{q} = 0$ for $q \geq q_{sat}$. Here the rhs of (9.12) gives of the dissipative, spring, and
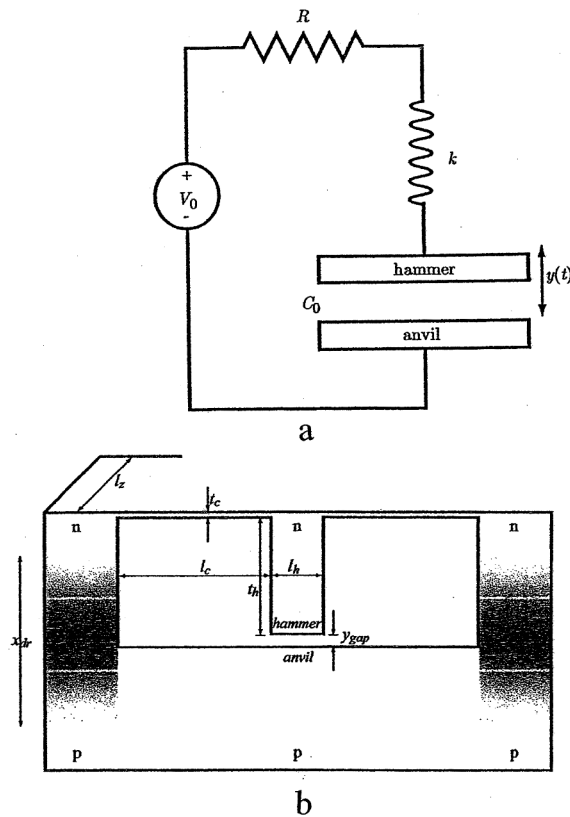
Figure 9.13: *Hammer-anvil* electromechanical oscillator. (a) macroscopic device schematic; (b) schematic of NEMS-MEMS device, with engineering dimensions.

electrostatic forces, respectively. q_{sat} is the maximum (saturated) charge on the plates, set by geometry and composition of the plates.

This system is electromechanically unstable: if the charged capacitor plates electrostatically draw together and electrically discharge, the attractive electric field collapses, the spring retracts the plates, the plates recharge on time scale τ_e, and the cycle can repeat. If the hammer's mechanical oscillation time constant $(\tau_m \sim 2\pi\sqrt{m/k})$ is comparable to the circuit's electrical time constant $(\tau_e \sim RC)$, and if the mechanical quality factor, Q_m, is sufficiently large, then the system can execute resonant, sustained electromechanical oscillation, converting electrical into mechanical energy.

A macroscopic laboratory model similar to Figure 9.13a was built and tested (scale length $\sim$ 50 cm); it validated the operating principles of this device. The model consisted of a 60 cm long tungsten spring (spring constant k = 0.8 N/m) attached to a mobile, circular capacitor plate (hammer, dia = 10 cm, m = 4 gm,
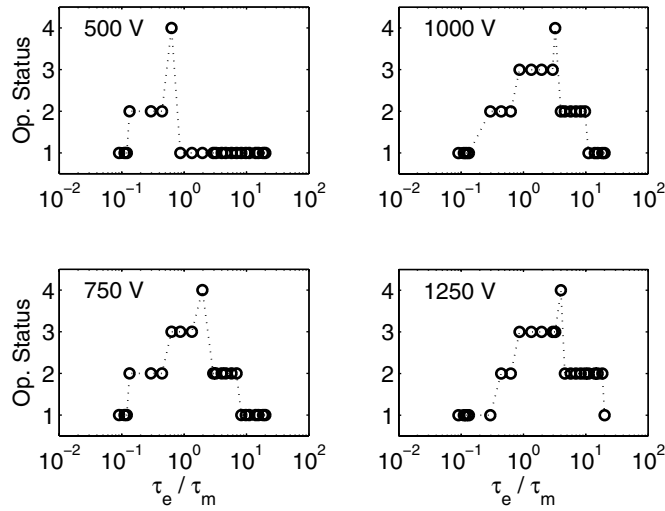
Figure 9.14: Operational status (OS) of macroscopic laboratory model *hammer-anvil* versus ratio of electrical and mechanical time constants (τ_e/τ_m). Legend: (1) no oscillation; (2) sub-harmonic or super-harmonic oscillation; (3) nearly harmonic oscillation; (4) harmonic oscillation. [19]

metallic), suspended above a fixed metallic plate, in series with a variable resistor ($5 \times 10^4 \Omega \leq R \leq 2 \times 10^7 \Omega$) and power supply ($500V \leq V_O \leq 2000V$). (A booster capacitor ($C_{boost} = 2\mu$ F) was placed in parallel with the *hammer-anvil* capacitor to allow $\tau_m \sim \tau_e$.) As the resistance R was varied and the resonance condition was met ($\tau_e \sim RC \simeq 2\pi\sqrt{\frac{m}{k}} \sim \tau_m$), the hammer-capacitor fell into steady-state oscillation, while outside this regime, the oscillation either could not be started or, if it was jump-started, the oscillation quickly died out.

Figure 9.14 depicts the operational status (OS) of the laboratory model at four bias voltages (500V, 750V, 1000V, 1250V). Operational status levels 1-4 on the ordinate correspond to: (1) no oscillation; (2) sub-harmonic or super-harmonic; (3) nearly harmonic; (4) harmonic oscillation. The abscissa gives the ratio of electrical to mechanical time constants (τ_e/τ_m), adjusted via the variable resistor R (Figure 9.13a). These are response curves comparable to those of typical forced resonant oscillators. As expected, Figure 9.14 indicates harmonic response (OS-3,4) at $\tau_e/\tau_m \sim 1$; and non-harmonic response elsewhere. The best resonance shifts to higher τ_e/τ_m values with increasing bias voltage. The OS-2 and OS-3 plateaus broaden with increasing bias voltage; this is consistent with the oscillator being driven harder and, thus, requiring less stringent (τ_e/τ_m) criterion to achieve gap closure. Similar peak broadening is predicted for the MEMS and NEMS *hammer-anvil*.

9.4.2 Operational Criteria

This macroscopic oscillator should scale down to the micro- and nanoscopic realms. Force equation (9.12) still applies, but with the addition of a van der Waals force term:

$$F_{vdW} = \frac{HA}{6\pi(y_{gap} - y)^3}, \tag{9.14}$$

where H is the Hamaker constant ($H = 0.4 - 4 \times 10^{-19}$J for most non-polar materials; for silicon $H_{Si} = 10^{-19}$J).

Consider the p-n device Figure 9.13b, a microscopic version of the *hammer-anvil*, consisting of two p-n diodes (columns) on either side connected on top to a block of n-type material suspended by two flexible cantilever springs over the central p-type base. Comparing Figures 9.13a and 9.13b, the top-center n-semiconductor mass in Fig 13b acts as the *hammer* in Figure 9.13a; likewise, the lower stationary p-semiconductor in Figure 9.13b acts as the lower, fixed *anvil*. The spring is replaced by a double cantilever. For long, thin cantilevers ($t_c \ll l_c$) and for small vertical displacements ($y_{gap} \ll l_c$), a linear spring constant can be defined: $k = \frac{Yl_z}{2}[\frac{t_c}{l_c}]^3$ where l_c, l_z, and t_c are length, width, and thickness, and Y is Young's modulus ($Y_{silicon} = 1.1 \times 10^{11}$N/m^2). The entire device can be regarded as a distributed network of resistors and capacitors; the long, thin cantilevers can dominate device resistance. The column depletion regions impose the built-in voltage across the central gap, similarly as for the p-n diode in Figure 9.1.

The electric field across its central gap provides negative electrostatic pressure which drives and sustains the mechanical oscillations. For sustained oscillation, three fundamental criteria must be met:

(i) The electrical and mechanical time constants must be comparable ($\tau_e \sim \tau_m$) to achieve electromechanical resonance.

(ii) The hammer's mechanical energy gain per cycle ($\Delta\mathcal{E}_{es}$) must equal or exceed its mechanical dissipation ($\Delta\mathcal{E}_{diss}$), otherwise the oscillation will damp out; and

(iii) The cantilever spring force retracting the hammer after contact with the anvil must exceed the maximum attractive forces (van der Waals + electrostatic), otherwise the hammer will stick to the anvil.

We will address each criterion separately, then combine (ii) and (iii) into a more general, combined criterion.

Criterion (i) ($\tau_e \sim \tau_m$): The electrical time constant τ_e for the p-n *hammer-anvil* junction (Figure 9.12b) should be on the order of the inverse-slew rate of a comparably-sized p-n diode. This is typically $10^{-6} - 10^{-8}$s for micron-size silicon diodes, corresponding to frequencies of $f \sim 1-100$MHz. The approximate resonant mechanical frequency of a double-cantilever is given by:

$$f_m \sim B_n\sqrt{\frac{Y}{\rho}}\frac{t_c}{l_c^2}, \tag{9.15}$$

where B_n is a constant of order unity, and ρ is the mass density of the cantilever ($\rho_{Si} = 2.3 \times 10^3$ kg/m^3). For comparison, a silicon cantilever of dimensions $t_c = 10^{-6}$m and $l_c = 10^{-5}$m should have a resonant frequency of approximately $f_m \sim 10^8$Hz. (The mass of the hammer could lower this frequency.)

Since f_m can be made comparable to f_e, the first criterion appears capable of being met by NEMS or MEMS systems. Mechanical resonant frequencies for cantilevers in excess of 10^9 Hz have been achieved, however, the quality factors (Q) of these are significantly reduced, possibly due to dissipative surface states which can dominate the physics at short distance scales [20, 21]. (For initial tests, f_e should be minimized so as to minimize f_m since this would imply physically larger devices, which are generally easier to fabricate and diagnose; also, larger devices imply larger Q_m, which should reduce power requirements.)

Criterion (ii) (Work versus dissipation): Criterion (ii) requires that the energy gained through electrostatic work on the hammer per mechanical cycle ($\Delta \mathcal{E}_{es}$) exceed the mechanical dissipation per cycle ($\Delta \mathcal{E}_{diss}$). The relatively small sizes of the electrostatic and dissipative forces compared with the mechanical spring forces allow use of the harmonic approximation, which yields a closed-form integral solution to the coupled equations (9.12) and (9.13). Thus, we assume the hammer executes lightly-damped ($Q \gg 1$) simple harmonic motion: $y(t) \simeq y_{gap}cos(\omega_o t)$, with $\omega_o = \sqrt{\frac{k}{m}}$. Substituting this into (9.13) yields an uncoupled equation for the evolution of the electric charge on the capacitor plates:

$$\dot{q} + q\frac{(1 - \cos(\omega_o t))}{RC_o} - \frac{V_o}{R} = 0 \tag{9.16}$$

whose solution for homogeneous initial conditions is found to be

$$q(t) =$$

$$\frac{V_o}{R} \exp[\kappa \sin(\frac{2\pi t}{\tau_m}) - \frac{t}{\tau_e}] \int_0^t \exp[\frac{\tau'}{\tau_e} - \kappa \sin(\frac{2\pi \tau'}{\tau_m})]d\tau' = \frac{V_o}{R} \exp[g(t)] \int_0^t \exp[-g(\tau')]d\tau', \tag{9.17}$$

where $\tau_m = 2\pi/\omega_o$, and $\kappa \equiv \frac{\tau_m}{2\pi\tau_e}$, and $g(t) = [\kappa \sin(\frac{2\pi t}{\tau_m}) - \frac{t}{\tau_e}]$. Here $\tau_e = RC_o$ need not be an RC time constant as for the macroscopic oscillator (Figure 13a); rather it will likely be set by microscopic thermal processes, for instance, charge carrier diffusion, generation and recombination rates. The type, doping, and temperature of the semiconductor should have a strong influence on τ_e; for example, GaAs should have significantly shorter time constants than Si.

The Gaussian parallel plate approximation $E = \frac{q}{\epsilon_o A}$ allows the electrostatic energy gain over one period of mechanical oscillation τ_m to be written as

$$\Delta \mathcal{E}_{es} = \oint F_{es} \cdot dy(t) = \int_0^{\tau_m} \frac{q^2(t)}{2\epsilon_o}[-\frac{1}{\tau_m}y_{gap}\sin(\frac{t}{\tau_m})]dt \tag{9.18}$$

Meanwhile, for lightly-damped oscillators ($Q_m \gg 1$), the dissipation can be expressed in terms of Q_m as:

$$\Delta E_{diss} \simeq \frac{\pi k y_{gap}^2}{Q_m} \tag{9.19}$$

Combining (9.18) and (9.19), the second criterion can be written:

$$\frac{\Delta \mathcal{E}_{es}}{\Delta \mathcal{E}_{diss}} = \frac{-Q}{2\pi\epsilon_o \tau_m k y_{gap}} \int_0^{\tau_m} q^2(t) \sin(\frac{t}{\tau_m}) dt. \qquad (9.20)$$

Resonant oscillation develops only for $\tau_e \sim \tau_m$. Away from this condition (either $\tau_m \gg \tau_e$ or $\tau_m \ll \tau_e$), it can be shown (taking $\tau_e \to 0$ or $\tau_e \to \infty$ in (9.17)) that the electric field becomes essentially static, so there is no net energy gain per cycle ($\Delta \mathcal{E}_{es} \longrightarrow 0$), while ΔE_{diss} remains constant (See (9.19).); thus the oscillation damps out. In the regime $\tau_e \sim \tau_m$, however, the asymmetry critical to resonance is realized: more work is performed *on* the spring by the field during gap closure than is work performed *by* the spring *against* the field on gap opening. It is also required that the Q of the oscillator is sufficiently large that the energy gain per cycle exceeds the energy loss per cycle. For lightly damped oscillators, oscillation can be sustained by minimal energy input.

Criterion (iii) (Non-stick hammer): The third criterion arises from the disparity in magnitude and spatial variation of the strengths of the forces acting on the hammer. For systems of interest, dissipative and electrostatic forces are subordinate to spring and van der Waals forces over the critical distances near where the hammer makes contact with the anvil. For the hammer not to stick to the anvil, the spring force at $y = y_{gap}$ must exceed the sum of the electrostatic and van der Waals (vdW) forces at the latter's cut-off (saturation) distance, typically $y_{cut-off} \sim 1.6 \times 10^{-10}$m, roughly an atomic radius. In this model, the dissipative and electrostatic forces act mechanically non-conservatively and can be of the same order of magnitude. The spring and vdW forces, on the other hand, are conservative and vary spatially with significantly different power laws and intrinsic strengths; while the spring force varies as $F_s \sim y$, the vdW force varies as $F_{vdW} \sim [y_{gap} - y]^{-3}$. Because of the latter's stronger spatial dependence, it can exceed the spring force at small gap distances – leading to stiction – unless steps are taken. Varying surface composition, one can alter the vdW force magnitude roughly over an order of magnitude via the Hamaker constant, but it can be most directly and easily reduced by reducing the contact area between the surfaces.

Since the parameter space for viable *hammer-anvil* oscillators is quite broad, for the sake of clarity and because experimental prototypes will most likely be pursued first in the MEMS regime, we will restrict much of the following discussion to parameters closely aligned with a well-known and specified MEMS production standard: the SUMMiT^{TM} process as developed and supported by Sandia National Laboratories.

In Color Plate VII the principal forces exerted on the hammer (excluding dissipation) are plotted versus gap opening for three typical oscillators, as specified by cantilever length (10-90μm). The electrostatic force is given for $V_o = V_{bi} = 0.6$V, with an electric field saturating at a maximum strength of 2×10^7V/m, similarly as for the p-n *standard device*. (This follows the conservative assumption that the vacuum gap electric field strength will remain below the dielectric strength of silicon (3×10^7V/m). It should also render a conservative (under-) estimate of actual device performance.) The vdW force is presented for five values of surface contact fraction ($10^{-4} \le \eta \le 1$). (For optimal designs of the *hammer-anvil*, η can

be up to about $\eta \simeq 10^{-2}$, indicating 1% direct physical contact between hammer and anvil surfaces.)

The third criterion can be written $F_s > F_{vdW} + F_{es}$, or

$$ky_{gap} > \frac{H\eta A}{6\pi y_{cut-off}^3} + \frac{\epsilon_o E_{max}^2 A}{2} \tag{9.21}$$

Since $F_{es} \ll F_{vdW}$ in the contact region, the third criterion can be reduced to:

$$\frac{6\pi ky_{gap}y_{cut-off}^3}{H\eta A} > 1 \tag{9.22}$$

If one sets the third criterion ((9.22)) to equality and combines it with the second criterion ((9.20)), one obtains a combined criterion

$$\frac{Q}{4\pi\epsilon_o^2 \tau_m ky_{gap}} \int_0^{\tau_m} q^2(t)\sin(\frac{t}{\tau_m})dt > 1 \tag{9.23}$$

If one extracts the dimensional term q^2 from the integrand, assumes the integral resolves to order one, and re-expresses slightly, then a general dimensionalized condition for steady-state operation of the oscillator can be written:

$$\frac{6\pi y_{cut-off}^3 \epsilon_o E_{max}^2 Q}{\eta H} \simeq \frac{Q}{\eta} \cdot \frac{\text{Electrostatic Pressure}}{\text{van der Waals Pressure}} > 1 \tag{9.24}$$

This general condition is the product of two simple ratios. The pressure ratio incorporates the pressure driving the oscillation (electrostatic) and the 'stiction pressure' (van der Waals), while the other ratio indicates the importance of minimum dissipation (Q) and minimum surface contact (η). Interestingly, the spring force, which figures prominently in both criteria (ii) and (iii), drops out of this combined criterion entirely.

9.4.3 Numerical Simulations

Numerical simulations using MatLab and commercial semiconductor device simulators verified the principal results of the 1-D model of the dc-driven resonant oscillator. Two-dimensional numerical simulations of the *hammer-anvil*, performed using Silvaco International's Semiconductor Device Simulation Software [Atlas (S-Pisces, Giga)], verified the equilibrium aspects of the system's electric field. Output from the simulations were the steady-state, simultaneous solutions to the Poisson, continuity, and force equations, using the Shockley-Read-Hall recombination model. Simulations verified that the magnitude of the open-gap electric field can exceed that of the local depletion region by almost an order of magnitude, topping out in excess of $2 \times 10^7 \text{V/m}$, similarly as for Color Plate IVb. Although the gap volume is significantly less than the depletion region volume ($y_{gap} \ll y_{dr}$), since electrostatic energy density is proportional to E^2, the electrostatic potential energy of the open gap can significantly exceed that of the depletion region. Numerical simulations also verified that the electric field and electrostatic energy in the gap

is lost upon gap closure as a new depletion region forms. Like the *standard device* earlier, the *hammer-anvil* constitutes a microcapacitor that can be discharged by gap closure.

The electrostatic pressure P_e for the open-gap *hammer-anvil* with even modest biasing (*e.g.*, $V_{bias} = 0.6$V) will be at least $P \sim 10^3$Pa. In principle, this can be supplied by the built-in potential, ($V_{bias} \equiv V_{bi}$). Although the absolute electro-static force exerted on the *hammer* is small, under Criteria (i-iii) it is sufficient to resonantly drive and maintain a high-Q oscillation. NEMS-MEMS cantilevers have documented Qs as high as $Q \sim 10^5$ in vacuum [20]. This implies that a small energy gain per cycle ($\sim 10^{-5}$ total mechanical energy) should be sufficient to sustain oscillation. In Plate VIII is plotted a range of viability for *hammer-anvil* devices constructed with physical dimensions achievable with the SUMMiT^{TM} process, and identical with the $l_c = 30\mu m$ case from Plate VII. Plate VIII presents minimum bias voltage required for sustained mechanical oscillation consistent with Criteria (i-iii) and realistic physical parameters for silicon based devices. Voltages are plotted as a function of quality factor Q and the ratio of electrical to mechanical time constants ($\frac{\tau_e}{\tau_m}$). Equipotentials (0.6V - 90V) are overlayed for comparison. Simulations are bounded above by the condition: $Q < 10^6$. Other areas not colored represent unviable regions of parameter space wherein the device requires a net input of reactive energy to oscillate, above and beyond the work required to offset presumed dissipation.

Plate VIII, as expected, indicates that the *hammer-anvil* performs most effi-ciently – *i.e.*, at the lowest dc-voltage – at the resonance condition ($\frac{\tau_e}{\tau_m} \sim 1$) and at large Q values. Away from these, either large driving voltages are required (*e.g.*, $V_o = 50$V for $\frac{\tau_e}{\tau_m} \sim 10^{-1}$, $Q \sim 10^3$) or else the device fails entirely (*e.g.*, $\frac{\tau_e}{\tau_m} \sim 20$, $Q \sim 10^4$). In the sweet spot of Plate VIII ($0.25 \leq \frac{\tau_e}{\tau_m} \leq 4$, $2 \times 10^3 \leq Q \leq 10^5$), the device can be driven at relatively low voltages (1V$\leq V_o \leq$5V) and should have a resonant electromechanical frequency of about $f \sim 1$MHz. Note it should be viable using $V_o = V_{bi} \simeq 0.6$V. This device is almost macroscopic in size (maximum dimension ~ 0.1mm) and can be fabricated within the current art of MEMS tech-nology. Analysis shows that this device should scale down well into the sub-micron regime and operate well at biases comparable to standard built-in voltages.

The most sensitive device dimensions and tolerances occur in the *hammer-anvil* gap. Optimal gap width will probably be less than 0.1 μm. The contacting surfaces must be highly parallel and their morphology must be tightly controlled so as to meet the condition of low contact fraction ($\eta \ll 1$). Contact wear is inevitable and may place limits on the total number of oscillations the device can execute [22, 23].

The *hammer-anvil* envisioned here will almost certainly require a kick start since the maximum achievable electrostatic pressure, although sufficient to sustain oscillation, appears insufficient to intitiate it. The kick start might be delivered in a number ways, including: a) a large, transient dc voltage spike across the gap; b) a small, short-lived, resonant, ac tickler voltage; or c) piezoelectric ac mechanical drive of the entire device. Device operation might be monitored either by laser interferometery of the hammer's motion, or by coupling its vibrational energy to piezolectric sensors. The latter would be propitious since, in principle, a piezo

could be used both to jump start the oscillation and also to detect it.

9.5 Experimental Prospects

Prospects are good for laboratory construction and testing of these solid-state electromechanical devices in the near future[2]. Present-day micro- and nano-manufacturing techniques are adequate to construct the necessary structures, however, the art of surface finishing, which is crucial to reducing friction and stiction, may not yet be adequate, particularly for the LEM. State-of-the-art molecular beam epitaxy can reliably deposit layers to monolayer precision, but control of surface states is still problematic. Self-assembly of the requisite surfaces is plausible. Large scale biotic systems (e.g., DNA, microtubules) are well-known to self-assemble with atomic precision, as are abiotic ones (e.g., carbon nanotubes [11, 12]). Molecularly catalysed construction (e.g., RNA to protein transcription inside ribosomes) is accomplished with atomic precision. Scanning tunneling microscopes have also been used to assemble complex systems atom by atom. In light of these accomplishments, it seems plausible that experimental tests of these solid-state challenges may be on the horizon. We predict laboratory tests for the LEM will become feasible within 5 years; tests of the *hammer-anvil* concept are feasible today. Such tests are currently being pursued by the USD group.

---

[2] *Capacitive Chemical Reactor*: One can also conceive of non-mechanical challenges emerging from the thermal capacitor concept [24]. Consider gas molecules, having ionization energies less than the work function of the semiconductor, infusing the J-II gap (Figure 9.1). The neutral gas molecules positively ionize at the positive gap surface (n-side), then desorb, at which time the gap electric field accelerates them across the gap up to superthermal energies ($qV_{bi} \gg kT$). (Likewise, gas molecules with large electron affinities could form negative ions at the p-side and accelerate in the opposite direction. Together, positive and negative ion fluxes would constitute a diffusion current that is otherwise forbidden by the vacuum gap.) The positive ion current is unidirectional since, with $qV_{bi} \gg kT$, once an ion crosses the gap it cannot return until it is neutralized. The ion kinetic energy is sufficient to drive chemical reactions (or at least catalyse them). In principle, low-energy chemical reactants can enter the capacitor gap and emerge as high-energy products. In this way, chemical energy can be created solely from heat (via the gap electrostatic energy) — this in conflict with the Kelvin-Planck form of the second law.

References

[1] Sheehan, D.P., Wright, J.H., and Putnam, A.R., Found. Phys. **32** 1557 (2002).

[2] Wright, J.H., *First International Conference on Quantum Limits to the Second Law*, AIP Conference Proceedings, Vol. 643, Sheehan, D.P., Editor (AIP Press, Melville, NY 2002) pg. 308; Putnam, A.R., *ibid.*, (2002) pg. 314.

[3] Wright, J.H., Sheehan, D.P., and Putnam, A.R., J. Nanosci. Nanotech. **3** 329 (2003).

[4] Sheehan, D.P., Phys. Plasmas **2**, 1893 (1995).

[5] Sheehan, D.P., Phys. Plasmas **3**, 104 (1996).

[6] Sheehan, D.P. and Means, J.D., Phys. Plasmas **5**, 2469 (1998).

[7] Yuan, J.S. and Liou, J.J. *Semiconductor Device Physics* (Plenum Press, New York, 1998).

[8] Neudeck, G.W. *Vol. II: The pn Junction Diode,* 2nd Ed., in *Modular Series on Solid State Devices*, Pierret, R.F. and Neudeck, G.W., Editors (Addison-Wesley, Reading, 1989).

[9] Trimmer, W., Editor, *Micromechanics and MEMS: Classic and Seminal Papers to 1990* (IEEE Press, New York, 1997).

[10] Meyer, E. and Overney, R.M., Dransfeld, K. and Gyalog, T. *Nanoscience* (World Scientific, Singapore, 1998) Chapters 3,5.

[11] Dresselhaus, M.S., Dresselhaus, G., and Avouris, P., Editors, *Carbon Nanotubes – Synthesis, Structure, Properties and Applications* (Springer-Verlag, Berlin, 2001).

[12] Harris, P.J.F., *Carbon Nanotubes and Related Structures* (Cambridge University Press, Cambridge, 1999).

[13] Cumings, J. and Zettl, A., Science **289** 602 (2000).

[14] Pathria, R.K., *Statistical Mechanics* (Pergamon, Oxford 1972) pp. 467-74.

[15] MacDonald N.C. in *Nanotechnology*, Timp, G., Editor (AIP-Springer Verlag, New York, 1999).

[16] Pelesko, J.A. and Bernstein, D.H., *Modeling MEMS and NEMS* (Chapman and Hall/CRC, Boca Raton, 2003).

[17] Roukes, M.L. in *Technical Digest of the 2000 Solid-State Sensor and Actuator Workshop*, Hilton Head Island, SC. (2000).

[18] Bienstman, J., Vandewalle, J., and Puers, R., Sensors and Actuators **A 66** 40 (1998).

[19] Perttu, E.K. and Sheehan, D.P., unpublished data (2003).

[20] Mohanty, P., Harrington, D.A., Ekinci, K.L., Yang, Y.T., Murphy, M.J., and Roukes, M.L., Phys. Rev. B **66**, 085416 (2002).

[21] Lifshitz, R. and Roukes, M.L., Phys. Rev. B **61**, 5600 (2000).

[22] Patton, S.T. and Zabinski, J.S., Tribology **35**, 373 (2001).

[23] Komvopoulos, K., Wear **2**, 305 (1996).

[24] Seideman, T. and Sheehan, D.P., private communication, *Frontiers of Quantum and Mesoscopic Thermodynamics*, Prague, Czech Republic (2004).